J Mater Sci (2008) 43:6301–6323
DOI 10.1007/s10853-008-2893-6

Development and verification of a meso-scale based dynamic material model for plain-woven single-ply ballistic fabric

M. Grujicic · W. C. Bell · T. He · B. A. Cheeseman

Received: 26 April 2008 / Accepted: 22 July 2008 / Published online: 16 August 2008

Abstract A meso-scale unit-cell based continuum material constitutive model has been developed for plain-woven single-ply ballistic fabric materials. This model, due to its computational efficiency, is suitable for use in computational analyses of the ballistic-protection performance of multi-layer body-armor vests. The model utilizes the continuum-level in-plane and out-of-plane deformation-state of the material, an energy minimization procedure and a simple account of yarn slip to update the structure/architecture of the fabric unit cell. Forces and moments developed within the structural components of the unit cell are then used to compute the continuum-level stress state at the material points associated with the unit cell in question. The model is implemented in a user-material subroutine suitable for use within commercial finite-element programs. To validate the model, a series of transient nonlinear dynamic analyses of the impact of a square-shaped fabric patch with a spherical projectile is carried out and the computed results compared with their counterparts obtained using a more traditional finite-element approach within which yarns and yarn weaving are modeled explicitly. The results obtained show that the material model provides a reasonably good description for the fabric deformation and fracture behavior under a variety of boundary conditions applied to fabric edges and under varying fictional conditions present at the yarn/yarn and projectile/fabric interfaces. In addition, the overall ballistic energy absorption capacity of the fabric as well as its yarn-strain energy, yarn-kinetic energy, and frictional sliding contributions are predicted with reasonable accuracy by the proposed material model for fabric.

M. Grujicic (✉) · W. C. Bell · T. He
International Center for Automotive Research CU-ICAR,
Department of Mechanical Engineering, Clemson University,
241 Engineering Innovation Building, Clemson, SC 29634, USA
e-mail: mica.grujicic@ces.clemson.edu

B. A. Cheeseman
Army Research Laboratory—Survivability Materials Branch,
Aberdeen, Proving Ground, MD 21005-5069, USA

Introduction

In recent years, there have been significant research efforts focused on the integration of woven fabrics with advanced technologies (such as flexible electronics, micro-fluidics, micro-actuators, etc.) to obtain hybrid woven systems with novel and unique capabilities [1]. Development of these technologies as well as the use of woven fabrics in apparel, fabric reinforced composites, and body armor for ballistic protection requires a thorough understanding of the mechanical behavior of these fabrics. In the present work, the quasi-static, in-plane, yarn-slip and yarn-failure free, meso-scale unit-cell based material model for plain-woven single-ply fabric initially developed by King et al. [2], has been enhanced for use in high deformation rate ballistic applications where yarn slip and failure are prevalent.

Over the last several years, military systems, in particular those supporting the US ground forces, are being continuously transformed to become faster, more agile, and more mobile so that they can be quickly transported to operations located throughout the world. As part of this transformation, an increased emphasis is being placed on the development of improved lightweight body-armor and lightweight vehicle-armor systems, as well as on the development of new high-performance armor materials. High-performance fiber-based materials have already been successfully exploited for both body-armor (e.g., as soft,

flexible fiber mats for personal-armor vests) and for the vehicle armor and structural systems (e.g., as reinforcements in flexible armor-grade and rigid structural-grade polymer matrix composites, *PMCs*).

Flexible lightweight materials have been used historically in body-armor systems to provide protection against specified threats, at reduced weight and without compromising person's mobility. Early materials used included leather, silk, metal chain mail and metal plates. Replacement of metal with a nylon (*poly-amide*) fabric and an E-glass fiber/ethyl cellulose composite in body-armor systems can be traced back to the Korean War [3]. Although, primarily due to their low cost, nylon and E-glass fibers are still being used today; high-performance polymeric fibers (typically used in the form of woven fabrics) are now the standard in most fiber-reinforced body-armor applications. To increase the ballistic performance of the body-armor vests, with respect to 0.30 caliber or small threats, ceramic insert strike-plates are commonly used [4].

The high-performance polymeric fibers used today are characterized by substantially improved strength, stiffness and energy-absorbing capacity. Among these high-performance fibers the most notable are: (a) *poly-aramids* (e.g., Kevlar®, Twaron®, Technora®); (b) highly oriented *poly-ethylene* (e.g., Spectra®, Dyneema®); (c) *poly-benzobis-oxazole*, PBO (e.g., Zylon®), and (d) *poly-pyridobisimi-dazole*, PIPD (e.g., M5®). When tested in tension, all these materials differ significantly from the nylon fibers, having very high absolute stiffness, extremely high density-normalized strength, and quite low (<4%) strains-to-failure. These fibers essentially behave, in tension, as rate-independent linear elastic materials. When tested in transverse compression, however, these fibers are similar to nylon and can undergo large plastic deformation without a significant loss in their tensile load-carrying capacity. This behavior is quite different from that found in carbon or glass fibers, which tend to shatter under transverse compression loading conditions. It should be also noted that an important functional requirement for the high-performance fiber used in ballistic-protection applications is their ability to withstand aggressive environmental conditions (e.g., high temperatures, high humidity, etc.). As an example, due to a loss of in their mechanical performance under high-temperature/high-humidity conditions, Zylon fibers are no longer approved for application in bullet proof vests.

Over the past two decades, there has been a great deal of work done on understanding the mechanical behavior of fabrics based on the high-performance fibers which are extensively employed in a variety of ballistic and impact protection applications. Nevertheless, the design of fabric-armor systems remains largely based on the employment of extensive experimental test programs, empiricism and old practices. While such experimental programs are critical for ensuring the utility and effectiveness of the armor systems, they are generally expensive, time-consuming and involve destructive testing. Consequently, there is a continuing effort to reduce the extent of these experimental test programs by complementing them with the corresponding computation-based engineering analyses and simulations.

Among the main computational engineering analyses used to model ballistic performance of flexible armor, the following main classes can be identified:

(a) Finite-element analyses based on the use of pin-jointed orthogonal bars to represent flexible fabric yarns. The most notable studies falling into this category of analyses are those performed by Roylance and Wang [5], Shim et al. [6], Lim et al. [7], Shahkarami et al. [8], Johnson et al. [9], and Billon and Robinson [10]. While the pin-jointed orthogonal-bars based finite-element analyses have proven to be very efficient in approximating the dynamic behavior of woven fabrics, the discrete nature of the yarn models was associated with inherent oversimplifications that significantly limited the predictive capability of the analyses. In particular, important contributions associated with the weave architecture, surface-finish and friction governed yarn-to-yarn and layer-to-layer contacts (in multi-layer fabrics) could not be accounted for;

(b) More-detailed full-blown 3D continuum finite-element analyses such as those carried out by Shockey et al. [11], Duan et al. [12–15], Zhang et al. [16], etc. have also been investigated. While these analyses have proven to be powerful tools for capturing and elucidating the detailed dynamic response of single-layer fabrics, they are computationally very demanding when applied to practical armor systems which typically contain 30–50 fabric layers/plies;

(c) Unit-cell based approaches have been used extensively in order to derive the equivalent (smeared) continuum-level (membrane/shell) material models of textile composites from the knowledge of the meso-scale fiber and yarn properties, fabric architecture, and inter-yarn and inter-ply frictional characteristics. Among the most notable studies based on these analyses are those carried out by Kawabata et al. [17–19] who introduced simple analytical models to capture the uniaxial, biaxial and shear behavior of fabrics. Furthermore, Ivanov and Tabiei [18] proposed a micro-mechanical material model for a woven fabric (in which a visco-elastic constitutive model was used to represent the mechanical behavior of the yarns) for the use in non-linear finite-element impact simulations. In deriving the material model, Ivanov and Tabiei [20] considered the motion of the yarn-crossover point and developed a procedure for

determining the equilibrium position of this point under the applied unit-cell strains. Recently, King et al. [2] proposed a new approach for deriving the continuum-level material model for fabrics based on the properties of the yarns and the weave architecture which involves the use of an energy minimization technique to establish the relationship between the configurations of the fabric structure to the microscopic deformation of fabric components. Similar unit-cell based continuum-level membrane/shell material models have been developed by Boisse et al. [21] and Peng and Cao [22]. Also, Shahkarami and Vaziri [23] proposed a similar but simpler model to that introduced by King et al. [2] and provided a detailed account of its incorporation into a material-model subroutine which can be readily coupled with commercial dynamic-explicit finite-element codes; and

(d) The use of higher-order membrane/shell finite-element analyses to represent the dynamic response of fabric under ballistic loading conditions and overcome the aforementioned computational cost associated with the use of full 3D finite element analyses of the yarn/fabric structure. Among the studies falling into this category, the most notable is the one carried out by Scott and Yen [24]. While the use of higher order membrane elements was found to be indeed advantageous computationally, it was never fully validated by comparing its results against either those obtained experimentally or those obtained using full 3D finite element analyses.

As pointed out above, while major efforts have been made in recent years to develop sophisticated numerical models capable of elucidating the ballistic performance of fabric armors, most of these models either lack computational efficiency or fail to capture many physical aspects of the yarn and fabric architecture and/or contact dynamic phenomena. Hence, the main objective of the present work is to develop an efficient shell-based meso-scale mechanics unit-cell based model that captures the essential dynamic/ballistic behavior of plain woven fabric under impact-loading conditions. The term "*meso-scale*" is used to denote yarn-level millimeter length scale details of the fabric microstructure/architecture. In other words, finer-scale molecular-level and fiber-level material details are not considered explicitly and instead only their lumped contributions are taken into account. The "*unit-cell*" term is used to denote the basic structural unit in a woven single-ply fabric so that a fabric patch can be considered as an in-plane assembly of such units. The material model developed in the present work is essentially an extension of the model recently proposed by King et al. [2] to include the effects of out-of-plane deformation, yarn slip and yarn failure.

The organization of the article is as follows: Details regarding the computational procedures employed to develop a new meso-scale unit-cell based material model for a prototypical plain-woven single-ply fabric and the implementation of this model into a material-user subroutine suitable for use in commercial finite-element programs are presented in the section "Development of the material model". The formulation of a simple projectile-armor impact problem used to validate the new material model is described in the section "Verification of the material model". Main results obtained in the current work are presented and discuss in the section "Results and discussion". The main summary points and conclusions resulting from the present work are listed in the section "Summary and conclusions".

Development of the material model

In this section and its subsections, a detailed account is given of the procedure used to develop the meso-scale unit-cell based continuum-material model for plain-woven single-ply fabric. Also, details regarding the implementation of the model into a material-user subroutine suitable for use in commercial finite-element packages are presented. The basic idea behind the unit-cell based approach is that the mechanical response of the fabric unit-cell (represented in terms of a number of structural members, e.g., trusses, springs, etc.) is smeared out into the equivalent response of a (anisotropic) continuum material. A simple schematic of the unit cell which is used to represent the plain-woven single-ply fabric structure/architecture allotted to a single yarn crossover is depicted in Fig. 1a. Its continuum-level material point counterpart is represented in Fig. 1b. Within the continuum-material framework, the yarns are not represented explicitly but rather by two material directions whose orientations are denoted in terms of material vectors, g_1 and g_2.

Coupling between the continuum-material formulation and the unit-cell geometry/architecture and mechanical response is done in the following way: (a) the deformation state of a continuum-material point (as quantified by the corresponding deformation gradient) is used to update the unit-cell geometry/architecture and the extent of yarn slip; (b) the updated unit-cell geometry/architecture and the extent of yarn slip are then used to compute the forces and moments acting on its structural members; and (c) the computed forces and moments along with their gradients through the shell thickness are next used to compute the associated stress state at the corresponding continuum-material point.

It must be noted that in order for the aforementioned approach to be valid (i.e., in order for homogenization of

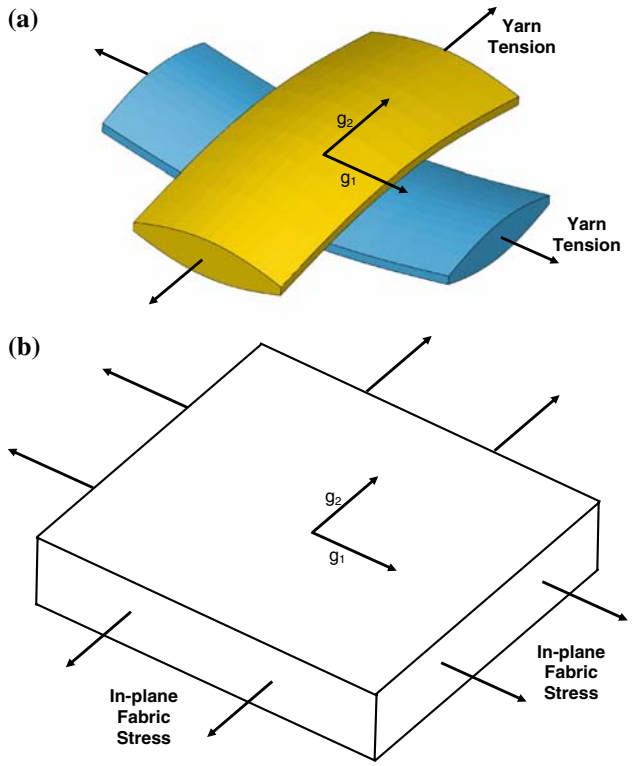

Fig. 1 The relationship between a fabric unit cell (**a**) and the corresponding material point in an anisotropic continuum (**b**)

the fabric unit-cell response to be justified), the characteristic length scale in the numerical analysis in which the model is used (e.g., the projectile and the fabric-patch sizes in a projectile/fabric impact problem analyzed in the present work) must be large in comparison to the fabric unit-cell edge length.

Fabric unit cell geometry/architecture

The geometry/architecture of the plain-woven single-ply fabric unit-cell used in the present work is displayed in Fig. 2. The warp and weft yarn segments within the unit-cell are each represented using two-member truss elements. To represent the yarn crimp arising from yarn weaving into the fabric, the truss elements do not lie in the plane of the fabric. Warp and weft yarn segments cross each other and interact at the crossover point. Yarn sliding will lead to the motion of this point. To allow for yarn stretching, truss elements have finite axial stiffness but their (out-of-plane) bending stiffness is set to infinity. Yarn out-of-plane bending is modeled as rotation of the two truss members of a yarn segment at the crossover point and the associated yarn-bending stiffness is accounted for through the use of a rotational spring attached to two truss members of the same yarn at the crossover point.

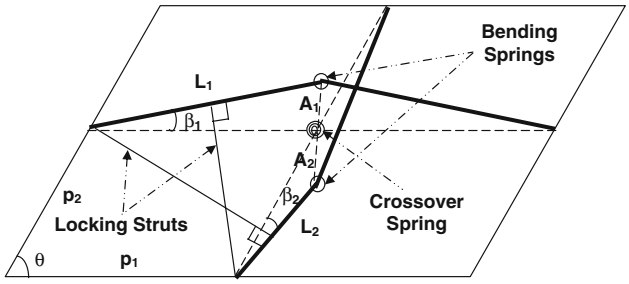

Fig. 2 The geometry/architecture of a plain-woven single-ply fabric unit cell used in the present work

Contacts and interactions between the warp and weft yarns at a crossover point in the direction normal to the plane of the fabric is modeled using a *"contact spring"* which provides elastic resistance towards the yarn crimp-amplitude reductions and the associated yarn cross-section changes.

Elastic and dissipative resistances towards the in-plane shear bending and the relative in-plane rotation of the warp and weft yarns in the presence of yarn/yarn friction is modeled using a rotational spring and a rotational damper, respectively.

Additional contacts and interactions between the warp and weft yarns can take place as a result of *"locking"*, a phenomenon which involves lateral compression (and the associated changes in the cross-sectional areas) of warp or weft yarns by the surrounding adjacent yarns of the other (warp or weft) family. As displayed in Fig. 3(a–c), this phenomenon can occur either as a result of a large in-plane shear deformation (*"shear locking"*) or as a result of large uniaxial tensile loading along the axis of one yarn family (*"cross locking"*). The cross-locking phenomenon is a result of *"crimp interchange"* (i.e., the fact that as the *"stretched"* yarns are being de-crimped, that is having their crimp amplitude decreased, the crimp amplitude of yarns of the other family is being increased and their crimp wave-length reduced). Since the unit-cell model used here does not track the yarn cross-sectional area changes, locking is modeled through the use of *"locking trusses"* which: (a) remain normal to the yarns of a given family (and, thus, the length of these trusses quantifies the distance between adjacent yarns of the same family); (b) allow the build-up of contact/locking forces between the yarns after the yarn locking conditions are met; and (c) provide increasingly higher unit-cell shear stiffness once the yarn locking conditions are met.

The geometry/architecture of the fabric unit-cell can then be described by the following 13 parameters (It should be noted that subscript *1* is used to denote warp yarns and *2* to denote weft yarns):

(a) The unit-cell half edge lengths, p_i ($i = 1, 2$)
(b) The yarn-segment/truss lengths, L_i ($i = 1, 2$)

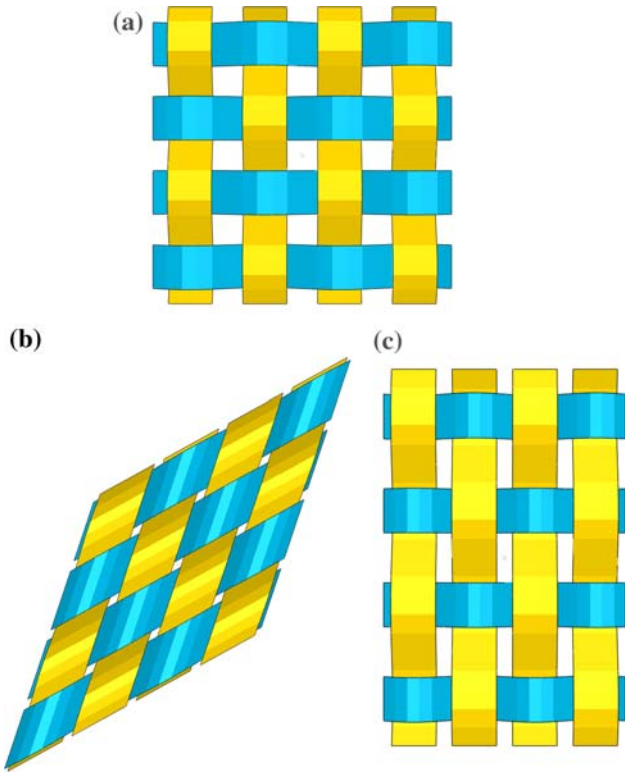

Fig. 3 The structure of a small fabric patch in: (**a**) its initial/undeformed configuration; (**b**) a state of shear-locking; and (**c**) a state of cross-locking

(c) The crimp angles, β_i ($i = 1, 2$)
(d) The crimp amplitudes, A_i ($i = 1, 2$)
(e) The locking truss lengths, d_i ($i = 1, 2$)
(f) The inclination angles of the locking trusses to the fabric plane, α_i ($i = 1, 2$) and
(g) The in-plane shear (i.e., warp-yarn/weft-yarn included) angle, θ.

To aid the reader in understanding the physical meaning of these parameters, they are identified—using the aforementioned notation—and clearly labeled in Fig. 2.

Out of the 13 parameters listed above only 5 are independent since simple geometrical relations exists between these parameters in a given configuration of the unit cell, e.g.:

$$A_i = \sqrt{L_i^2 - p_i^2} \quad (i = 1, 2), \tag{1}$$

$$\cos\,\beta_i = \frac{p_i}{L_i} \quad (i = 1, 2), \tag{2}$$

$$d_i = \sqrt{p_i^2 \sin^2\theta + A_j^2 \xi_j^2} \quad for (i,j) \in \{1,2\}, i \neq j, \quad (i = 1, 2), \tag{3}$$

$$\alpha_i = \tan^{-1}\left(\frac{A_j \xi_j}{p_i \sin\theta}\right) \quad (i = 1, 2), \text{and} \tag{4}$$

$$\xi_j = \left|1 - \frac{|p_i \cos\theta|}{p_j}\right| \quad for\ |p_i \cos\theta| \leq 2p_j \quad (i = 1, 2) \tag{5}$$

In the remainder of the work, the two unit-cell edge lengths, p_i, the two yarn lengths, L_i, and the in-plane warp-yarn/weft-yarn included angle, θ, will be considered as the independent variables needed to fully describe the geometry and the architecture of the unit-cell.

Constitutive relations for unit-cell structural components

As presented in the previous section, the fabric architecture and behavior within a unit-cell is described in terms of a number of structural elements, e.g., the two-member trusses, bending springs, contact springs, etc. In this section, the corresponding mechanical constitutive relations are defined for all the elements. These relations are necessary for computation of the forces/moments acquired by these components during deformation as well as of the associated energy storage/dissipation.

Yarn tension

Tension within the truss members, T_i, is described by the following linear-elastic rate-independent relation:

$$T_i = K_i\left(L_i - L_{0,i}\right) \quad (i = 1, 2) \tag{6}$$

where subscript 0 is used to denote the initial (undeformed) quantity, and K_i is the yarn-stiffness constant. The truss members have no ability to support compressive axial loads.

Yarn bending

The yarn-bending moment, M_{bi}, is assumed to depend linearly on the change in yarn crimp angle, $\beta_i - \beta_{0,i}$, so that the constitutive relation for the rotational springs attached at the truss-member pin joints is defined as:

$$M_{bi} = K_{bi}\left(\beta_i - \beta_{0,i}\right) \quad (i = 1, 2) \tag{7}$$

where K_{bi} is the bending stiffness. To account for different amounts of permanent set in the yarns, appropriate values should be assigned to the reference crimp angle $\beta_{0,i}$.

Yarns crossover contact

Yarn/yarn interactions and yarn cross-sectional area changes at the crossover points are accounted for through the use of a non-linear, axial *"interference"* spring whose contact force, F_I, versus yarn-interference, d_I, relation is defined by the following constitutive relation:

$$F_I = \frac{K_I d_I}{1 - d_I/a} \tag{8}$$

where K_I and a are the spring constant and the interference upper bound, respectively, and the interference, d_I, is defined as a difference between the sum of the initial crimp amplitudes and the sum of the current crimp amplitudes. To describe yarn/yarn interactions, a concept of yarn interference is used. Yarn interference is defined as a condition when the center-to-center distance of two contacting crossing-yarns becomes smaller than the sum of the initial half-thicknesses of these yarns. Eq. 8 models a *"soft"* yarn contact/interaction behavior in which a negative interference yields a minimal *"pulling"* force, while at positive-interference values the interaction is initially quite compliant and becomes stiffer as the interference increases.

Yarn locking

Before a constitutive relation for the locking trusses is proposed, it must be recognized that the yarn cross section is typically an oblate ellipse. Yarn cross-sectional area changes associated with the crossover-point interference, discussed above, are taking place primarily in the direction of the minor axis of the yarn cross-section (i.e., in the fabric through-the thickness direction). In the case of yarn locking, these changes take place in a direction parallel with the yarn cross-section major axis. Consequently, the locking response is expected to be more compliant than the yarn crossover-interference response. To account for this difference, a power-law relation is used to describe the locking force, $F_{L,i}$, versus locking interference, $I_{L,i} = d_{0,i} - d_i$, where $d_{0,i}$ is the locking-truss length where the locking first time takes place.

$$F_{L,i} = \begin{cases} 0 & I_{L,i} \le 0 \\ K_d (I_{L,i})^c & I_{L,i} > 0 \end{cases} \tag{9}$$

where K_d and c are the *"locking"* material parameters. It should be noted from Eq. 9 that the locking trusses do not develop any locking force in tension.

Yarn shear bending

As mentioned earlier, in-plane shear of the fabric is the result of relative rotation of the warp and weft yarns at the crossover points (known as *''trellising''*) and of in-plane yarn bending. Typically, in-plane shear stiffness of the fabric increases with an increase in the in-plane shear strain (i.e., with an increase in the warp-yarn/weft-yarn *"yarn-included"* angle, θ) as yarn locking begins to develop. Since the contribution of yarn locking to the fabric response has been accounted for through the use of the locking trusses, only the additional elastic (due to yarn bending at the crossover points) and dissipative (frictional losses due to yarn rotations at the crossover points) components of the in-plane fabric shear remain to be addressed.

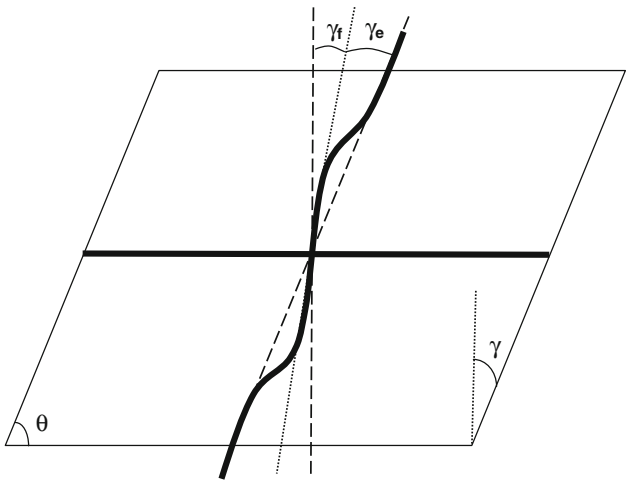

Fig. 4 Decomposition of the relative yarn rotation angle $\gamma = \pi/2 - \theta$ into its elastic, γ_e, and frictional-dissipative, γ_f, components

A schematic of the yarn bending and rotation at the crossover points is displayed in Fig. 4. For clarity, the two yarns are drawn in the same plane, (the plane of fabric) and one of them is kept straight. As seen, the yarn-included angle $\gamma = \pi/2 - \theta$ can be decomposed into the elastic γ_e and frictional γ_f components. The two components are related to the bending moment, M, developed at the yarn-crossover point as:

$$M = K_s \gamma_e \tag{10}$$

and

$$M = M_0 \left(\frac{\dot{\gamma}_f}{\dot{\gamma}_0} \right)^{1/b} \tag{11}$$

where K_s is an elastic bending stiffness and M_0, $\dot{\gamma}_0$, and b are the rate-dependent power-law coefficients which are considered as constants (although they may, in general, depend on the deformation state of fabric).

During verification of the meso-scale unit-cell material model it was found that the viscous-friction based relation, Eq. 11, had to be replaced with a rate-independent equation since ABAQUS/Explicit does not support a viscous friction model. To overcome this problem, for a typical shear-strain rate of 10^3 s^{-1} encountered during ballistic testing of the fabric, an average partitioning of γ into γ_e and γ_f as a function of γ was determined. This procedure yielded the following relationship between γ_e and γ: $\gamma_e = (0.01\gamma)/(0.01 + \gamma)$. This simplification was found not to significantly affect the computational results obtained using the meso-scale unit-cell based model.

Determination of the current unit-cell geometry and architecture

As discussed in the section "Fabric unit cell geometry/architecture", five independent geometrical parameters are needed to fully describe the current geometry/architecture of the unit-cell. In this section it is shown how these parameters are related to the continuum-level deformation state of the material point corresponding to the unit-cell in question.

At the continuum level, the state of deformation at a given material point is described by the deformation gradient, F, whose components in a Cartesian coordinate system are defined as:

$$F_{jk}(t) = \frac{dx_j(t)}{dX_k} \tag{12}$$

where $x_j(t)$ is the j th component of a material point at time t, and X_k the k th component of the same point in the initial/un-deformed configuration.

At the continuum level, the warp and the weft yarns can be described using vectors p_i ($i = 1, 2$) aligned with the axis of these yarns and the length of these vectors can be set equal to the corresponding current unit-cell edge lengths, p_i ($i = 1, 2$). These vectors can be related to their initial counterparts, $p_{0,i}$ ($i = 1, 2$) as:

$$p_i = Fp_{0,i} \quad (i = 1, 2) \tag{13}$$

The lengths of p_i ($i = 1, 2$) can be defined as:

$$p_i = \sqrt{p_i \cdot p_i} = \sqrt{(Fp_{0,i}) \cdot (Fp_{0,i})} = \sqrt{p_{0,i}(F^{\mathrm{T}}F)p_{0,i}} \tag{14}$$

where the yarn-included angle θ can be computed from:

$$p_1 \cdot p_2 = (Fp_{0,1}) \cdot (Fp_{0,2}) = p_1 p_2 \cos\theta \tag{15}$$

Under the condition that no slip occurs between yarns at the crossover point, so that the location of the crossover point is related to the unit-cell deformation in an affine manner, Eqs. 14 and 15 also represent the unit-cell edge lengths and the yarn included angle at the meso-scale unit-cell level. Thus, three unit-cell geometrical parameters, p_i ($i = 1, 2$), and θ, can be obtained from the continuum-level deformation gradient of a point associated with the unit-cell in question. The remaining two parameters, L_i ($i = 1, 2$), are not defined at this point. In other words, there is an infinite number of unit-cell configurations which can be associated with a given (continuum-level) deformation state. However, different configurations will be associated with different levels of the (internal) elastic stored energy. To determine the *"unique"* unit-cell configuration associated with a given deformation state, an energy argument is used. That is, it is postulated that the unit-cell will acquire the geometry/architecture associated with a lowest level of the elastic stored energy. To determine this unique structure of the unit-cell, a standard optimization algorithm can be used, as discussed below.

Within the optimization procedure used in the present work, the *"objective function"* (i.e., the total elastic stored energy within the unit cell at a given state of deformation, as defined by the current deformation gradient) is minimized with respect to the *"design variables"* (i.e., the two truss lengths, L_1 and L_2). Toward that end, the total strain energy stored in the trusses (due to yarn extension), bending springs (due to yarn bending), and yarn-crossover spring (due to yarn-crossover contacts and bending) is first expressed as a function of the L_1 and L_2. This was done by summing the individual stored energy components, each of which is obtained by integrating the force/moment over the loading path of the structural member in question. Then starting with initial guess values for the L_1 and L_2, these two parameters are varied in a systematic manner (using an optimization algorithm) in order to determine their values which minimize the total elastic energy stored in the unit cell. Since the objective function possesses only one minimum in a realistic range of values for L_1 and L_2, a local optimization algorithm could be used. The Downhill Simplex optimization algorithm [25] was selected since it does not require the evaluation of the derivatives of the objective function which makes it computationally very efficient. It should be noted, that the term *optimization* used in this section pertains to a procedure used to determine the unique (minimum energy) structure of the unit-cell, and not to a procedure which is used to determine an optimal architecture of the fabric with respect to its ballistic-protection performance.

It should be also noted that, as pointed out by one of the reviewers of the present manuscript, the optimization procedure utilized in this section is of a local nature and, hence, does not necessarily correspond to the global minimum energy condition (the condition corresponding to the minimum energy of the system with respect to the truss length of all the unit-cells in the model. While the latter non-local optimization procedure could be used and implemented into the same user subroutine developed in the present work, this was not done because the associated computational cost was found to be prohibitively high. To confirm the fidelity of the present optimization scheme, few computational analyses were carried out using the global optimization approach and no significant differences between the corresponding two sets of results were found.

Determination of the material-point in-plane stress state

Once the current geometry/architecture of the unit cell is determined (i.e., once L_1 and L_2 corresponding to the

minimum elastic stored energy are computed), forces and moments acting on different structural members at the faces of the unit cell can be computed using the appropriate constitutive relations. These in turn, can be used to compute the in-plane stress state at the material point associated with the unit cell in question. It should be noted that the *"true"* measure of the stress state in the deformed configuration of a material point is the Cauchy stress, σ. To compute the stress state, the following relation is used between the traction-force vector, t, resulting from σ and acting on a small surface element dS with a unit normal n:

$$t = n\sigma dS \tag{16}$$

Thus, if the forces/moments acting on each structural member of the unit cell are used to compute the traction force acting on each of the unit cell faces in the current configuration, then Eq. 16 can be used to compute the corresponding in-plane material point stresses. Using this procedure the following expression for the stress tensor at a given material point is obtained:

$$\begin{aligned}\sigma = &\frac{1}{2p_2\sin\theta}\left(T_1\cos\beta_1 - \frac{M_{b1}\sin\beta_1}{L_1} - \frac{M\cos\theta}{2p_1\sin\theta} - \frac{F_{L1}p_1}{d_1} - F_{L2}\left(\frac{p_2^2\cos^2\theta}{p_1d_2} + \frac{p_2\sin\alpha_2|\cos\theta|\sin\beta_1}{L_1}\right)\right)(g_1\otimes g_1)\\ &+\frac{1}{2p_1\sin\theta}\left(T_2\cos\beta_2 - \frac{M_{b2}\sin\beta_2}{L_2} - \frac{M\cos\theta}{2p_2\sin\theta} - \frac{F_{L2}p_2}{d_2} - F_{L1}\left(\frac{p_1^2\cos^2\theta}{p_2d_1} + \frac{p_1\sin\alpha_1|\cos\theta|\sin\beta_2}{L_2}\right)\right)(g_2\otimes g_2)\\ &+\left(\frac{M}{4p_1p_2\sin^2\theta} + \frac{F_{L1}p_1\cos\theta}{2p_2d_1\sin\theta} + \frac{F_{L2}p_2\cos\theta}{2p_1d_2\sin\theta}\right)(g_1\otimes g_2 + g_2\otimes g_1)\end{aligned} \tag{17}$$

where g_1 and g_2 are unit vectors aligned with the current orientation of the two yarns and symbol $\otimes$ is used to denote a tensorial product of two vectors. It should be noted that as seen in Eq. 17, the stress state at a given material point has contributions from the yarn tensions, T_i, yarn-bending moments, M_{bi}, locking forces, F_{Li}, and the inter-yarn bending moment, M.

Furthermore, it must be noted that Eq. 14 does not include the effect of yarn slip to the in-plane stresses. This effect is added in the section "Yarn slip at the crossover points".

To summarize, the (in-plane) Cauchy stress tensor for a given unit cell is computed using the following procedure: (a) The forces that all load-bearing meso-structural members exert on the unit-cell faces are computed first; (b) The components of these forces that lie in the plane of the fabric are determined next; (c) These forces are then resolved along the yarn directions, designated by unit vectors g_i; (d) The resolved forces are next divided by the appropriate projected areas to obtain stresses and the results are expressed in tensorial form in terms of the yarn direction vectors g_i; and (e) finally, it is ensured that the resulting stress tensor is symmetric.

Out-of-plane behavior of the fabric

The unit-cell material model developed in the previous section describes only the in-plane fabric behavior, the behavior which is dominated by in-plane stretching along the yarn directions and the inter-yarn rotation-induced in-plane shear. When plain-woven fabric is modeled using shell finite elements then, in addition to the in-plane fabric behavior, one must also define the out-of-plane fabric behavior. The out-of-plane behavior includes: (a) the through-the-thickness compression; (b) two transverse shears; (c) two out-of-plane bending modes; and (d) fabric twist deformation mode. In the remainder of this section, contributions of the six aforementioned out-of-plane deformation modes to the stress state at a given material point are presented and discussed.

Through-the-thickness compression

The through-the-thickness compression is resisted by the cross-over axial interference spring whose constitutive behavior is described by Eq. 8. Since the in-plane tensions/yarn-decrypting are also resisted by the same spring, and the in-plane tensions do not induce through-the-thickness stresses, one must determine the additional compressive displacement experienced by the spring due to through-the-thicknesses compression before the through-the-thickness normal compressive stress can be calculated (by dividing the additional contact force as defined by Eq. 8 by the current unit-cell surface area).

Transverse shear

Within ABAQUS/Explicit finite element program [26] used in the present work, only a linear-elastic transverse shear response of the fabric can be defined (which requires specification of two transverse shear stiffness moduli) and

this must be done within the main finite-element model/analysis input file (outside of the VUMAT user-material subroutine used for implementation of the current material model). The two transverse-shear stiffness moduli are set to relatively large values which ensures that the contribution of transverse shear to the overall deformation behavior of the fabric is relatively small (i.e., approaches the Kirchoff-Love shell bending limit) in accordance with typical experimental observations [27].

Out-of-plane bending

Since within the VUMAT user-material subroutine, the stress state is assessed for each shell element at a number of material points with equal in-plane coordinates and different through-the-thickness locations, the effect of out-of-plane bending is (at least partly) accounted for by the in-plane material model developed in the previous section. That is, the effect of bending-induced through-the-shell-thickness tension gradient is included in the in-plane fabric response. However, the effect of the fabric's principal curvatures within the given unit cell is not taken into account. The effect of shell curvature is accounted for by adding the following term to the in-plane stress state (as defined by Eq. 17) for all material points of a given shell element:

$$\sigma_{oop} = \frac{1}{2p_2 \sin\theta}\left(\frac{M_{oop,1}}{p_1}\right)(g_1 \otimes g_1) + \frac{1}{2p_1 \sin\theta}\left(\frac{M_{oop,2}}{p_2}\right)(g_2 \otimes g_2) \tag{18}$$

where the out-of-plane bending stiffness, $K_{oop,i}$, is used to relate, in a linear fashion, the out-of-plane bending moment, $M_{oop,i}$, and the principal curvature, κ_i. The principal curvatures are computed using the through-the-thickness gradient of the corresponding in-plane normal strains.

Fabric twist deformation mode

While the pure out-of-plane bending discussed above is associated with a through-the-thickness gradient of in-plane normal tensile strains, fabric twist is caused by the through-the-thickness gradient in the in-plane shear strain. The resulting twisting-moment, M_{twist}, gives rise to the following contribution to the stress state, Eq. 17:

$$\sigma_{\text{twist}} = \left(\frac{M_{\text{twist}}}{4p_1p_2 \sin^2\theta}\right)(g_1 \otimes g_2 + g_2 \otimes g_1) \tag{19}$$

where the out-of-plane twist stiffness, K_{twist}, is used to relate, in a linear fashion, the out-of-plane twisting-moment, M_{twist}, and the twist angle, ϕ_{twist}. The twist angle is computed using the through-the-thickness gradient of the in-plane shear strains.

Yarn slip at the crossover points

The meso-scale unit-cell based material model for plain-weave fabric presented in the previous two sections was based on an assumption that no yarn slip takes place at the yarn/yarn-crossover points. In other words, an affine deformation is assumed to take place within each unit cell. This assumption leads, in general, to an over-estimation of the stress levels (in highly stressed fabric regions) by the unit-cell model relative to the stress levels obtained in computational analyses in which yarns and their weaving/crimp are represented explicitly. In the latter analyses, slip of yarns at the crossover points is generally found to make significant contributions to the deformation response of fabric during impact with a high-velocity projectile. To overcome the aforementioned shortcoming of the present meso-scale unit-cell based material model, a procedure was devised to account for yarn slip. Details of this procedure are presented in the remainder of this section.

Slip of a yarn at the crossover point is caused by differences in the tension along the length of that yarn. Differences in the yarn-slip velocities at three adjacent crossover points of a yarn, lead to differences in the velocities at which the yarn material enters (v_{in}) and leaves (v_{out}) the unit cell associated with the middle crossover point. The latter differences give rise to a change in the un-loaded length of the yarn segments allotted to the unit cell in question. The rate of change of this length, $\dot{L}_{i,0}$, can be defined as follows:

$$\dot{L}_{i,0} = y_{i,0}(v_{\text{in}} - v_{\text{out}})\frac{L_{i,0}}{L_i} \tag{20}$$

where the $L_{i,0}/L_i$ term is used to remove the effect of tension-induced yarn-segment length extension. The velocities at which the yarn material enters ($v_{\underline{\text{in}}}$) and leaves ($v_{\text{out}}$) a unit cell are generally assumed to scale with the power of tension difference across the unit-cell boundary in question via a viscous-drag type relation in the form:

$$v = v_0\left(\frac{\Delta T}{\Delta T_0}\right)^m \tag{21}$$

where v_0, ΔT_0, and m are material/contact parameters while v and ΔT are the conjugate yarn-material velocity difference and the yarn tension difference, respectively.

Equations 20 and 21 show that when the yarn tensions at three adjacent crossover points are known, the rate of change of the un-loaded yarn segment length in the unit cell associated with the middle crossover point can be calculated. Integration of this change over a given time increment yields the corresponding change in the un-loaded yarn segment length and, in turn, to the current value of the un-loaded yarn-segment length. The latter quantity is

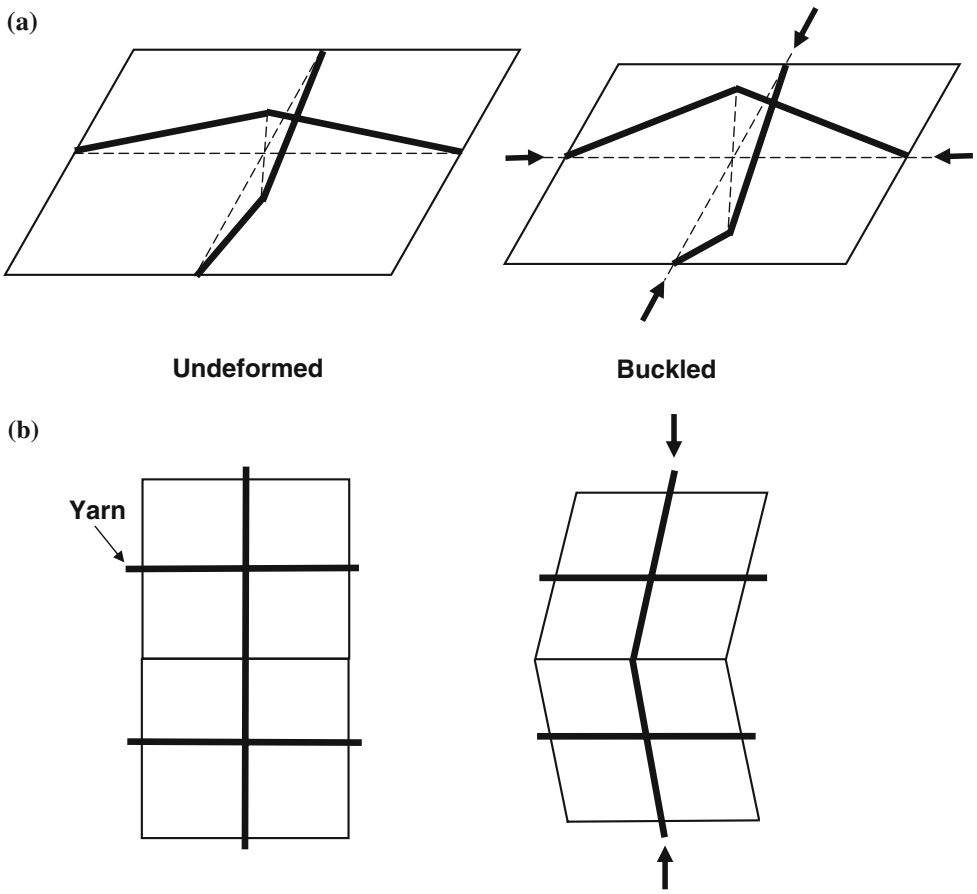

Fig. 5 Two common fabric buckling modes: (**a**) the *"yarn buckling"* mode (isometric view); and (**b**) the *"shear buckling"* mode (top view)

then used in Eq. 6 to calculate the corresponding slip-corrected yarn-segment tension in the unit-cell in question.

Fabric buckling

The fabric unit-cell model displayed in Fig. 2 is stable only under tension even when it is constrained to remain planar. When subjected to compression, the fabric unit cell is unstable and can, in general, buckle in one of the two following modes: (a) yarns can undergo bending at the crossover points and increase their crimp ("*yarn buckling*"), Fig. 5a; or b the yarns can rotate about axes perpendicular to the fabric plane, causing a shearing motion of the fabric ("*shear buckling*"), Fig. 5b. The dynamic finite-element analysis used in the present work to model fabric impact by a projectile has a shortcoming that it includes the rigid-body inertial resistance of the center of mass of the unit-cell, but not the inertial resistance to the relative rigid body motions of meso-scale structural elements of the unit-cell. To overcome this shortcoming, inertial resistance to yarn rotation is added explicitly to the meso-scale model developed here. This was done by dividing the changes of both the in-plane and the out-of-plane rotational velocities of the yarns by the current time increment to determine the corresponding average rotational accelerations. The reaction forces and moments corresponding to these rotational accelerations are then added to the previously defined *"static"* forces and moments and used in Eq. 17. In should be also noted that due to the presence of the rotational interference spring at the crossover point, the fabric buckling via the yarn-buckling mode is less likely to take place.

Failure of yarns

When the unit cell is stretched in a particular in-plane direction, the corresponding yarn is either de-crimped/straightened or stretched. In the former case, no tension is built within the yarn, while in the latter case tension is created within the yarn and, if sufficiently high, can cause yarn failure. Also, the extent of tension in a given yarn is affected by the failure status of the other crossing yarn. If the crossing yarn is not broken and is in contact with the stretched yarn, tension will develop in the two yarns, the extent of which is dependent on the crossover-point interference and the unit-cell dimensions and shape. In the present work, yarn failure is assumed to be load controlled,

i.e., a yarn is broken instantaneously when its tensile load reaches or exceeds a critical value.

Parameterization of the material model

Before the meso-scale unit-cell model developed in the present work can be implemented, the values of all its parameters must be determined. Due to the space limitations, only a brief description of the procedure used for model parameterization is presented in this section. The model parameters for a prototypical Kevlar® 129 balanced plain-woven fabric analyzed in the work of Duan et al. [12] were assessed as follows:

(a) Truss stiffness K in Eq. 6 is determined from the knowledge of the yarn axial modulus and the yarn cross-sectional area;

(b) Rotational spring stiffness K_b in Eq. 7 is computed from the knowledge of the bending stiffness of non-interacting bundled fibers (a lower bound), the bending stiffness of a yarn consisting of transversely fully coupled fibers (an upper bound) and a lateral fiber-interaction factor;

(c) Yarn-crossover parameters K_I and a in Eq. 8 were determined by carrying out a finite-element analyses of a compression test of a stack of fabric patches in which yarns and their weaving are represented explicitly;

(d) In-plane bending stiffness, K_s, in Eq. 10 and viscous-shear parameters, $M_0\left(\frac{1}{\dot{\gamma}_0}\right)^{1/b}$ and b were determined by carrying out a FEM analysis of the shear-frame test in which a square patch of the fabric (with the yarns running in the $\pm 45^{o}$ directions) is clamped along the four edges and pulled in the diagonal direction. The resulting force versus displacement curve is next matched using the meso-scale unit-cell model and a least-squares based curve-fitting procedure;

(e) The out-of-plane fabric bending modulus, K_{oop} used to evaluate M_{oop} in Eq. 18 is determined by carrying out a FEM analysis of the 3-point bending test of a fabric patch. The resulting moment versus curvature data are matched using the current meso-scale unit-cell model and the aforementioned curve-fitting procedure;

(f) The twist stiffness, K_{twist}, used to evaluate M_{twist} in Eq. 19 is determined by carrying out a FEM analysis of a twist test of a piece of fabric. The resulting moment versus twist angle results are matched using the meso-scale unit-cell model and the aforementioned curve-fitting procedure;

(g) $v_0\left(\frac{1}{\Delta T_0}\right)^m$ and m slip parameters in Eq. 21 were taken from the work of King [27];

(h) Failure loads for the yarn were taken from the work of Duan et al. [12]; and

(i) Translational and rotational inertia parameters of the yarn segments were determined using their basic geometrical characteristics and density of the yarns.

A summary of the meso-scale unit-cell based material model parameters used in the present work is given in Table 1.

Table 1 Miso-scale unit-cell material model parameters used in the present work

Parameter	Symbol	Value	Unit	Assessment procedure used
Truss stiffness	K	1.60×10^{-7}	N/m	$K = EA/L$
Rotational spring stiffness	K_b	$K_{b\_\text{lower}} = 6.68 \times 10^{-8}$ $K_{b\_\text{uper}} = 1.07 \times 10^{-5}$ $f = 0.055$ $K_b = 7.87 \times 10^{-6}$	Nm/radian	$K_{b\_\text{lower}} = 12NEI_{\text{fiber}}$ $K_{b\_\text{uper}} = 12EI_{\text{yarn}}$ $K_b = K_{b\_\text{lower}} + f(K_{b\_\text{lower}} + K_{b\_\text{uper}})$
Interference relation coefficient	K_I	3.09×10^{-3}	N	FEM analysis of shear sandwich test
Interference relation exponent	a	1×10^{6}	1/m	
In-plane bending stiffness	K_s	0.0131	Nm/radian	FEM analysis of shear frame test
Viscous-shear parameters	M_0	3.2×10^{-6}	Nm	
Reference dissipative rotation rate	$\dot{\gamma}_0$	0.00284	Radians/s	
Dissipative rotation rate sensitivity	b	4.0	–	
Locking stiffness	K_d	1.36×10^{13}	N/m^c	
Locking exponent	c	3.70	–	
Out-of-plane fabric bending modulus	K_{oop}	3.40×10^{-7}	Nm^2	FEM analysis of 3-poind bending test
Twist stiffness	K_{twist}	1.0×10^{-3}	Nm/radian	FEM analysis of twist test
Material/Contact parameters	$v_0/(\Delta T_0)^m$	7.91×10^{-11}	$\text{m/(sN}^m\text{)}$	Taken from the work of King
	m	1.107	–	

Material model implementation in a user-material subroutine

The meso-scale unit-cell based material model described in the previous section is next implemented in the material-user subroutine, VUMAT, of the commercial finite-element program ABAQUS/Explicit [26]. This subroutine is compiled and linked with the finite-element solver and enables ABAQUS/Explicit to obtain the needed information regarding the state of the material and the material mechanical response during each time step, for each integration point of each element. In the present work first-order 4-node general-purpose reduced-integration shell elements (ABAQUS/Explicit designation S4R) are used. Due to the use of the Simpson's numerical-integration method for the calculation of through-the-thickness deformation response of the shell, an odd number (greater than 1) of integration points has to be used in the through-the-thickness direction. The results obtained in the present work suggest that selecting three integration points provides a good compromise between computational efficiency and accuracy.

The essential features of the coupling between the ABAQUS/Explicit finite-element solver and the VUMAT material-user subroutine at each time increment at each integration point of each element can be summarized as follows:

(a) The corresponding previous time-increment stresses and material state variables as well as the current time-step deformation gradient are provided by the ABAQUS/Explicit finite-element solver to the material subroutine. In the present work truss lengths, and yarn failure and element-deletion status flags were used as the state variables; and

(b) Using the information provided in (a), and the meso-scale unit-cell user material model presented in the previous section, the material stress state as well as values of the material state variable(s) at the end of the time increment are determined within the VUMAT and returned to the ABAQUS/Explicit finite-element solver. In addition, the changes in the total internal and the inelastic energies (where appropriate) are computed and returned to the solver. It should be also noted that due to the presence of in-plane and out-of-plane gradient terms in the material model, global three-dimensional matrices containing tension, normal in-plane strains or shear in-plane strains had to be assembled and used during each call of the VUMAT subroutine.

It should be recalled that within the VUMAT only the normal and shear in-plane and through-the-shell-thickness compression responses of the material are computed. Transverse shear stiffness of the shell elements has to be defined as part of the overall FEM model definition outside the VUMAT. Using the provided values for the transverse shear modulus, ABAQUS/Explicit uses a simple procedure in which the transverse response of a shell is approximated by the transverse response of an analogous solid finite element.

It should be also noted, that the VUMAT file developed in the present work could be used with minor modifications and new parameterization for a variety of woven ballistic fabric materials and architectures.

Verification of the material model

As stated earlier, the main objective of the present work was to develop a fabric-structure/architecture dependent and physically based, computationally efficient material model which can be used in ballistic-protection performance analyses of multi-ply body armor. The verification of the model is presented in this section. Ideally, model validation is conducted by comparing model predictions with their experimental counterparts. Unfortunately, no relevant experimental/field-test data were available so the following alternate model validation approach was adopted. That is, the same problem, a simple projectile/armor impact problem, is analyzed computationally using two approaches: (a) a finite-element analysis in which the ballistic fabric was represented using the meso-scale material model developed in the present work; and (b) a more-accurate yet computationally more-costly finite-element analysis in which fabric yarns and their weaving was accounted for explicitly. In the section "Introduction", four different categories of computational analyses of the ballistic-protection performance of fabric were identified. Among these four categories, the one associated with explicit representation of fabric yarns and their weaving is associated with the least model reduction and is hence deemed most accurate. Therefore, this type of analysis was used here to carry out verification of the present meso-scale unit-cell material model.

The initial configurations of the projectile/armor finite-element systems analyzed here are shown in Fig. 6a and b. In both cases, a rigid spherical projectile with a 4 mm radius and a 2.12 g weight is propelled at an initial velocity of 300 m/s in the direction normal to the single-ply armor surface and toward the center-point of the armor. The armor is modeled as a 32.8 mm by 32.8 mm square single-ply fabric patch.

In Fig. 6a, the plain-woven fabric structure is modeled explicitly by snaking through orthogonally oriented warp and weft yarns. The square-shaped fabric patch contained 40 warp and 40 weft yarns. Yarns are considered to have a constant 0.040 mm^2 hexagonal cross-sectional area. The

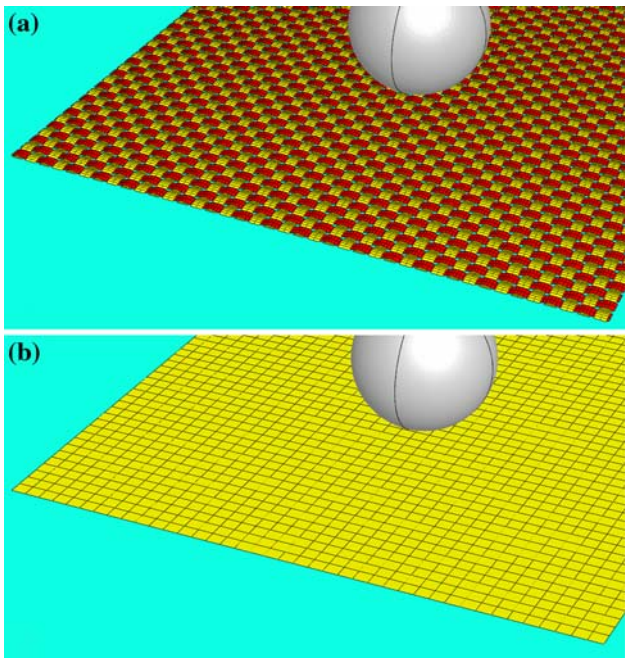

Fig. 6 The initial configurations of the projectile/fabric systems for (**a**) a shell FEM analysis in which yarn weaving is modeled explicitly; and (**b**) a shell FEM analysis in which the effects of yarn weaving are included implicitly through the use of an meso-scale unit-cell based material model

hexagonal cross section was used since this is the best approximation to the actual elliptical cross section which can be obtained using two-element wide yarns and the *"Nodal Thickness"* option available in ABAQUS/Explicit. The yarn width is set to 0.615 mm, the peak height to 0.105 mm, the crimp height to 0.088 mm and crimp wavelength to 1.64 mm. All these values are consistent with those used by Duan et al. [12–15] and, for an effective yarn density of 0.6 g/cm^3, they yield an effective fabric areal-density of 3.31 g/cm^2. The yarn material is assumed to be linear-elastic orthotropic (or more precisely, transversely isotropic) with the unique material direction being aligned with the yarn-axis direction). The orthotropic linear-elastic yarn-material properties used are listed in Table 2 and they relate to the corresponding properties of Kevlar® 129. Low values for the transverse normal and shear moduli and for the Poisson's ratios (listed in Table 2) arise from the fact that the fibers bundled within yarns are only weakly coupled to each other. In the remainder of the manuscript, the analysis involving the model displayed in Fig. 6a will be referred to as the *yarn-level FEM analysis*.

In the case of Fig. 6b, the armor is modeled as a constant-thickness shell-based continuous surface. In other words, warp and weft yarns and their weaving are not modeled explicitly. The effect of yarn weaving, however, is included implicitly through the use of the meso-scale unit-cell based material model (presented in the section "Development of the material model") which was assigned to each shell element of the fabric in Fig. 6b. In the remainder of the manuscript, the analysis involving the model displayed in Fig. 6b will be referred to as the *unit-cell based FEM analysis*.

Three different types of far-field boundary conditions applied to the edges of the fabric patch were considered: (a) all four fabric edges are clamped; (b) two opposite fabric edges are clamped and the other two are free; (c) all four fabric edges are set free.

A simple penalty-based algorithm is used to model yarn/yarn and projectile/fabric interactions. A Coulomb model was used to analyze yarn/yarn and projectile/fabric friction. Two frictional conditions were considered: (a) both the yarn/yarn friction coefficient $\mu_{y/y}$ and the projectile/fabric friction coefficient $\mu_{p/f}$ are set to 0.5; and (b) no yarn/yarn or projectile/fabric friction.

Due to explicit account of the warp and weft yarns and their weaving which entails the use of finer meshes, the FEM model displayed in Fig. 6a is typically computationally 2–3 times more expensive than the one displayed in Fig. 6b.

To validate the meso-scale unit-cell based material model, the interaction between the projectile and the armor is analyzed using the two FEM models and two aspects of these interactions are closely examined: (a) The residual velocity of the projectile after the projectile has successfully penetrated the armor; and (b) the extent, the temporal evolution and the spatial distribution of fabric-armor deformation and damage. It should be noted that the impact of a projectile with the fabric is associated with the initiation of several phenomena which were analyzed in details in our recent work [28]. In the same work, a detailed overview was given of the three main projectile kinetic-energy absorbing mechanisms, i.e.: (a) yarn-strain energy; (b) yarn-kinetic energy; and (c) the energy lost due to frictional sliding. It should also be noted that in Ref. [28], the ballistic fabric was modeled as a collection of explicitly defined interwoven yarns, and that no meso-scale material model or the concept of the unit-cell was used. The resulting model was found to be computationally quite

Table 2 The orthotropic linear elastic material data for Kevlar® 129 yarns [11] used in the present yarn-level finite element analyses

E_{11} (GPa)	E_{22} (GPa)	E_{33} (GPa)	G_{12} (GPa)	G_{13} (GPa)	G_{23} (GPa)	ν_{12}	ν_{13}	ν_{23}
164.0	3.28	3.28	3.28	3.28	3.28	0.0	0.0	0.0

expensive, which is one of the key motivations for the development of the present meso-scale unit-cell based material model.

Results and discussion

As mentioned earlier, the primary purpose of the present work was to develop, implement and validate a computationally efficient, meso-scale unit-cell based material model for plain-woven single-ply fabric armor. Since the key functional requirement for an armor system is to absorb the kinetic energy carried by the projectile, a quantitative comparison of the results pertaining to the temporal evolution of the absorbed energies (through yarn deformation and fracture, fabric acceleration and frictional-sliding based energy dissipation) obtained using the two FEM formulations (discussed in the previous section) is presented in this section and its sections. First, the results obtained for the case of far-field boundary conditions corresponding to the case when all four fabric edges are clamped, and for the two frictional conditions are presented and discussed. Next, results showing the effects of far-field boundary conditions are presented and analyzed.

Clamped fabric edges boundary condition

In this section, the results for two FEM analyses are presented for the case of fixed boundary conditions being applied to all four edges of the fabric. Since it is well established that yarn/yarn friction and projectile/fabric friction may play an important role in fabric's ability to absorb the projectile kinetic energy [e.g., 29], two frictional conditions were considered: (a) Both the yarn/yarn friction coefficient $\mu_{y/y}$ and the projectile/fabric friction coefficient $\mu_{p/f}$ are set to a non-zero (=0.5) value; and (b) A zero friction condition.

Fabric deformation and yarn fracture in the presence of friction

When a projectile hits the armor, two elastic-stress waves are generated: (a) a longitudinal wave which travels away from the point of impact along the principal yarns (the yarns directly hit by the projectile) and along those secondary yarns (the yarns not directly impacted by the projectile) which are interacting with the principal yarns. Propagation of the longitudinal wave outward from the point of impact enables a large fraction of the fabric armor to undergo deformation and, thus, absorb the kinetic energy of the projectile; and (b) a transverse wave which propagates outward from the point of impact at a velocity substantially lower than the sound speed and is responsible for stretching of the principal and the *"engaged"* secondary yarns. Since the sound speed is controlled by the yarn axial stiffness and density, and these two quantities are identical in the two FEM models, the temporal and spatial evolutions of the longitudinal-wave front are found to be quite comparable in the two models (the results not shown for brevity). On the other hand, the temporal evolution and the spatial distribution of the transverse-wave front are, in general, affected to a greater extent by yarn/yarn interactions. Therefore, a comparison of the transverse-deflection wave-front propagation results obtained using the two FEM analyses can be considered as a good validity test for the meso-scale unit-cell based material model developed in the present work.

Examples of the temporal evolution of deformation within the fabric obtained using the yarn-level FEM analysis and the unit-cell based FEM analysis are displayed in Figs. 7a–d and 8a–d, respectively. In these figures, side and top views of the fabric along with superimposed contour plots of the transverse displacement (the displacement normal to the fabric surface) are shown. A simple comparison of the results displayed in Figs. 7a–d and 8a–d reveals that the temporal evolution of the deformation state of fabric is quite similar in the two analyses and can be summarized as follows:

(a) Initially, the shape of the transverse-deflection wave-front in the fabric is nearly circular in both analyses and, thus, essentially identical to the shape of the projectile/fabric contact-zone, Figs. 7a and 8a;
(b) In the case of the yarn-level FEM analysis, as the time proceeds, the transverse-deflection wave generated within the principal yarns (the yarns which are in direct contact with the projectile) propagates outward and, through their interactions with the secondary yarns (the yarns which are not in direct contact with the projectile), at the yarn crossovers, cause the secondary yarns to also deflect in the transverse direction. Consequently, the transverse-wave front begins to acquire a near square shape (with the square diagonals extending in the warp-/weft-yarn directions), with the square center coinciding with the impact-zone center, Fig. 7b and c. In the case of the unit-cell based FEM analysis, the fabric is modeled as a continuous surface and, hence, the transverse wave can propagate in all in-plane directions from its source point (i.e., from the point of initial impact). However, since the in-plane load transfer is carried out via the yarn trusses, the transverse wave-front still acquires a square-like shape Fig. 8b and c;
(c) The extent of the transverse wave-front propagation and the magnitudes of the corresponding deflections are quite comparable in the two FEM analyses;

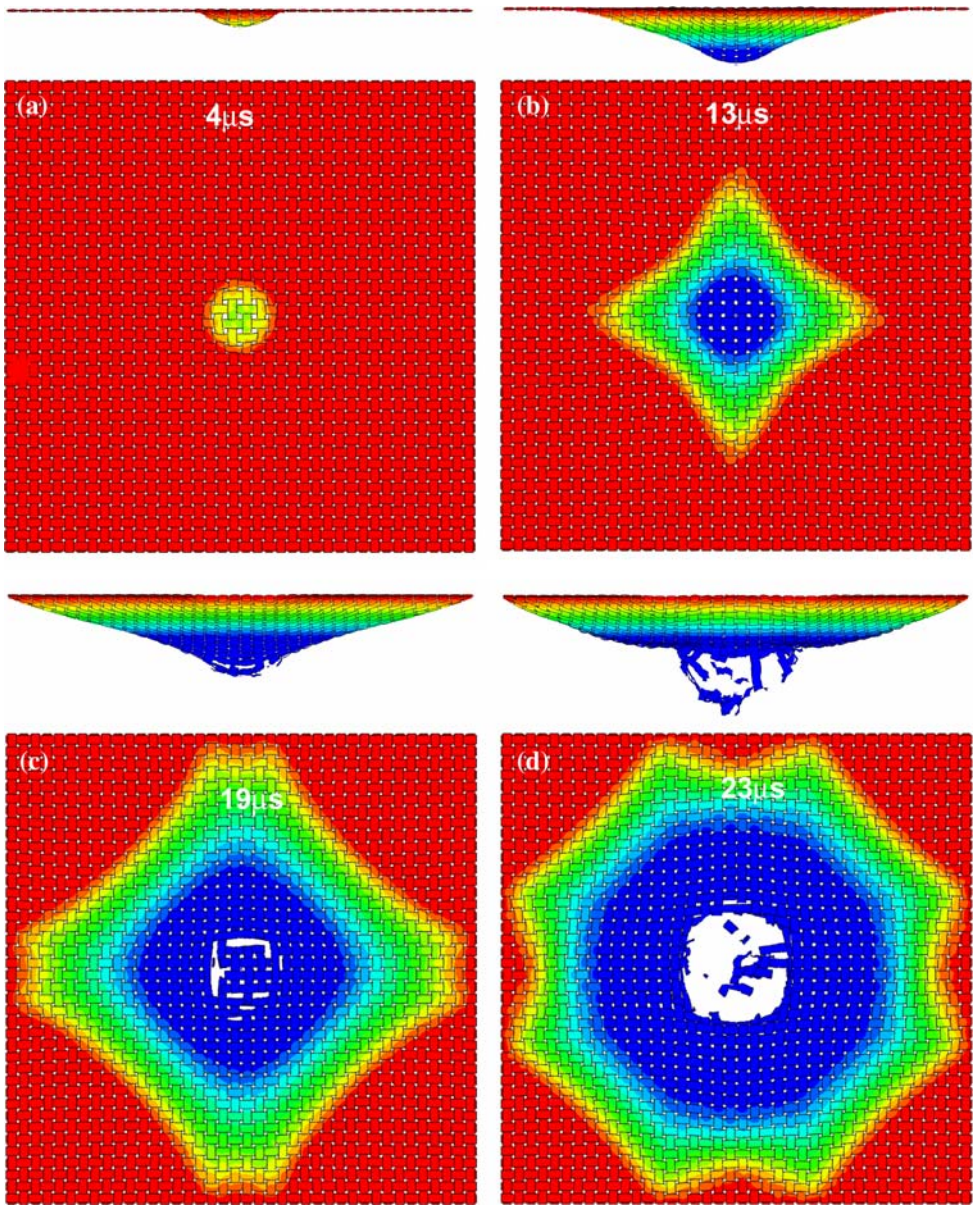

Fig. 7 The temporal evolution of deformation in the fabric for the yarn-level FEM model under the yarn/yarn $\mu_{y/y}$ and projectile/fabric $\mu_{p/f}$ friction coefficients of 0.5. Contour bands correspond to different values of the transverse displacement, i.e., the displacements normal to the fabric surface. All four fabric edges are fixed

(d) Upon reaching the clamped edges of the fabric, the square-shaped transverse-deflection wave-front is reflected back towards the center of the impact zone and the wave front acquires an octagonal shape, Figs. 7d and 8d.

(e) The first evidence of fabric failure is seen in the case of the yarn-based FEM analysis, Fig. 7c. In the case of the unit-cell based FEM analysis, yarn failure occurs at approximately equal post-impact time, Fig. 8c. It should be noted that the agreement between the results displayed in Figs. 7c and 8c is better than it appears. In Fig. 8c yarn failure in one direction has taken place in a number of finite elements, however these elements were not deleted, as element-deletion criterion requires yarn failure in two directions;

(f) The final fabric penetration-hole size appears to be smaller in the case of unit-cell analysis, Fig. 8d, than in the yarn-level based case, Fig. 7d. This apparent discrepancy can be related to the element-deletion criteria used in the present work, as discussed in point (e);

(g) At ~25–27 μs, the projectile completely penetrates the fabric and continues to move at a residual velocity of 290.2 m/s in the case of yarn-level FEM analysis and at a velocity of 289.2 m/s in the case of unit-cell based FEM analysis; and

(h) It should be noted that despite the fact that the projectile/fabric model has two vertical planes of symmetry, the damage region is slightly asymmetric in both types of analyses. The reason for this is that

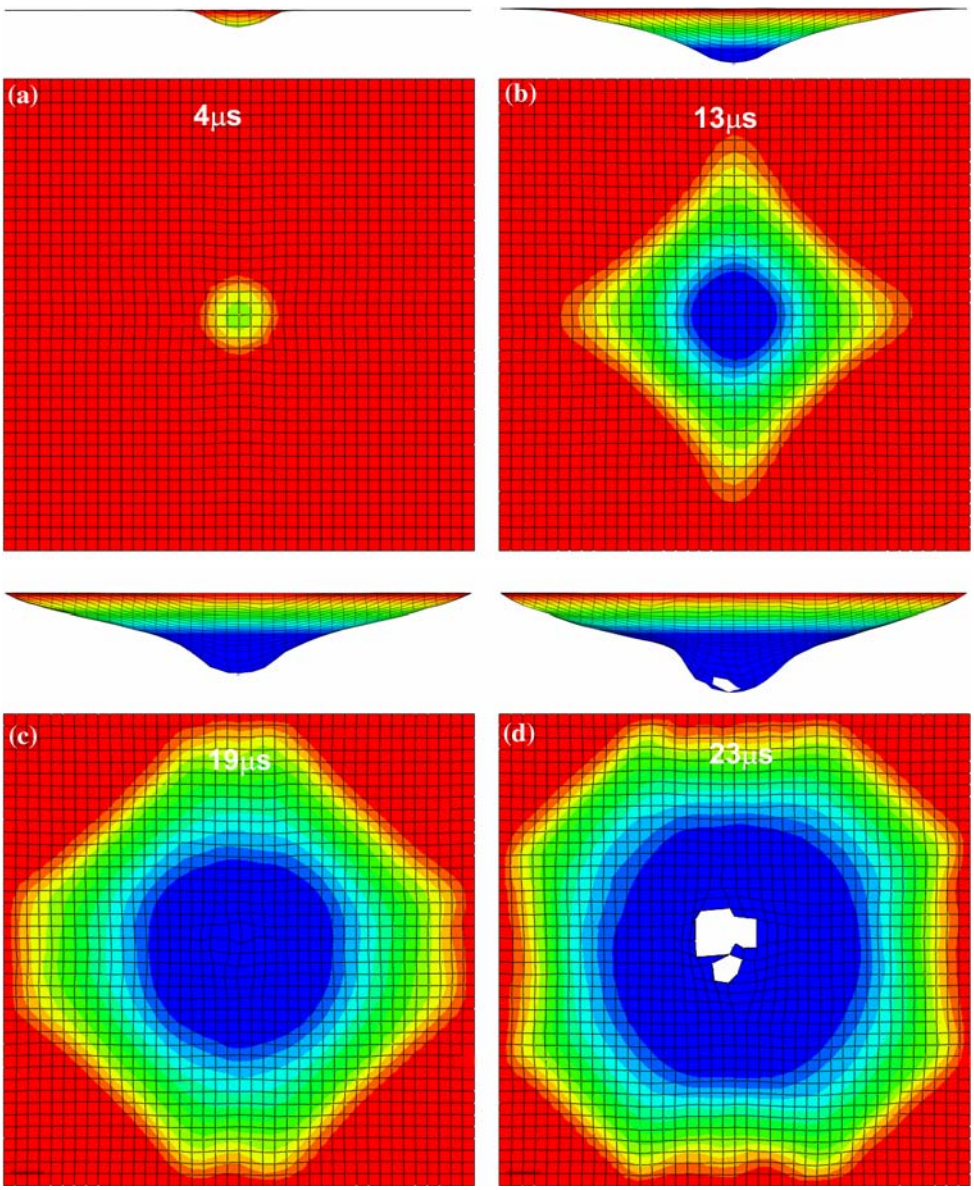

Fig. 8 The temporal evolution of deformation in the fabric for the unit-cell based FEM model under the yarn/yarn $\mu_{y/y}$ and projectile/fabric $\mu_{p/f}$ friction coefficients of 0.5. Contour bands correspond to different values of the transverse displacement, i.e., the displacements normal to the fabric surface. All four fabric edges are fixed

the finite-element discretization of the projectile into tetrahedron elements did not possess two planes of symmetry. The results displayed in Figs. 7a–d and 8a–d thus also reveal the effect of small geometrical perturbations in the (spherical) projectile on the fabric failure response.

Fabric deformation and yarn fracture in the absence of friction

The results displayed in Figs. 7a–d and 8a–d and their discussion presented in the previous section clearly establish that, at the yarn/yarn and projectile/yarn friction-coefficient conditions of 0.5, the two FEM analyses yield comparable results regarding the temporal evolution of the deformation and failure within the fabric during impact. In this section, the corresponding computational results obtained using the two FEM analyses for the case of zero yarn/yarn and projectile/fabric friction conditions are presented and discussed.

Examples of the temporal evolution of deformation within the fabric obtained using the yarn-level and the unit-cell based FEM analyses in the absence of yarn/yarn and projectile/fabric friction are displayed in Figs. 9a–d and 10a–d, respectively. In these figures, side and top views of the fabric along with superimposed contour plots of the transverse displacement are shown. A simple comparison of the corresponding results reveals that the temporal evolutions of the deformation state of fabric are quite similar in the two FEM analyses at shorter post-impact times, Figs. 9a,b and 10a,b, respectively. At longer post-impact

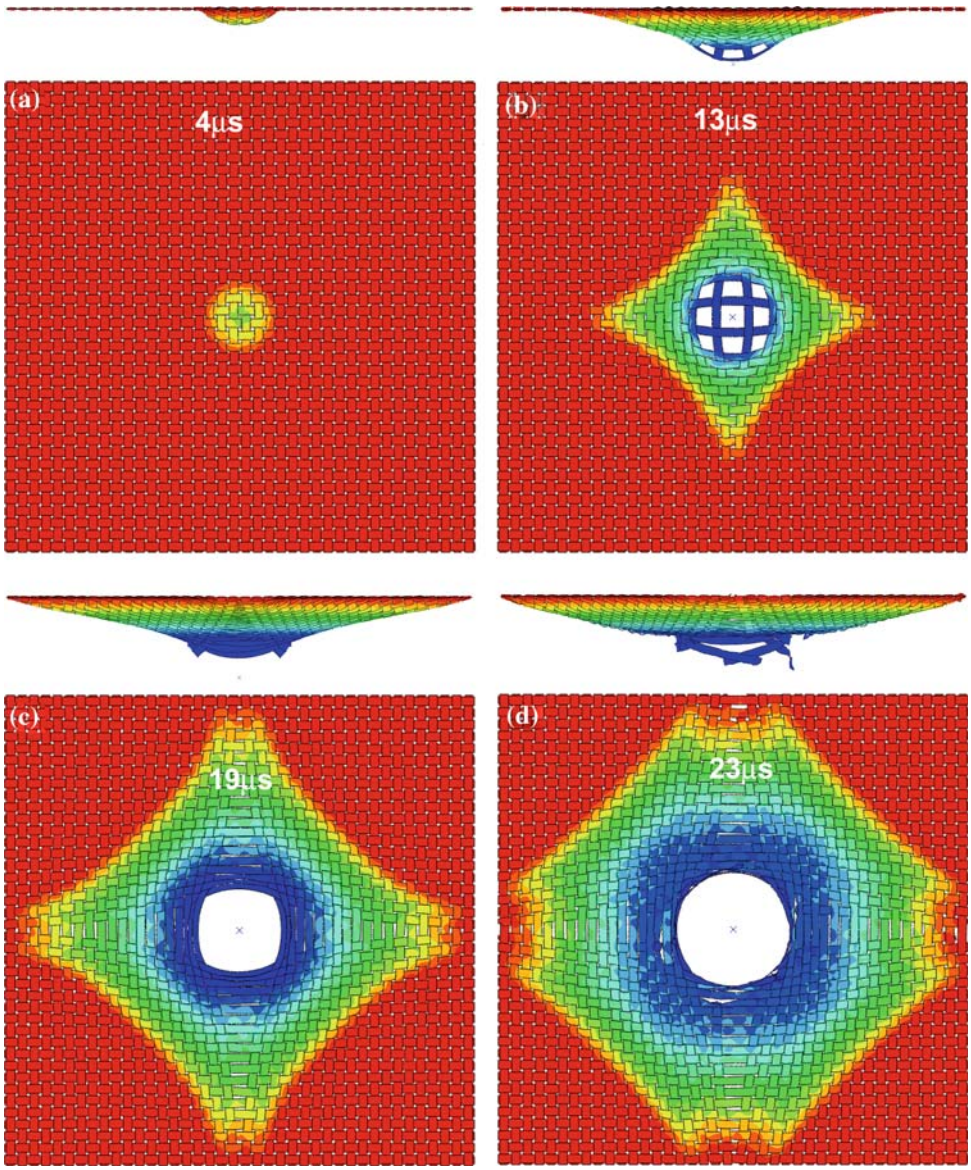

Fig. 9 The temporal evolution of deformation in the fabric for the yarn-level FEM model under the yarn/yarn $\mu_{y/y}$ and projectile/fabric $\mu_{p/f}$ friction coefficients of 0.0. Contour bands correspond to different values of the transverse displacement, i.e., the displacements normal to the fabric surface. All four fabric edges are fixed

times, Figs. 9c,d and 10c,d, the agreement is less satisfactory. The main reason for the observed discrepancy is that in the yarn-level FEM analysis, the principal yarns can readily move sideways to avoid the projectile, while such yarn mobility in the unit-cell based analysis was accounted for through the yarn-slip model. Since yarn-slip model enables yarn mobility along the length of the yarn and not in a transverse direction, more yarn movement and less yarn breaking takes place in the yarn-based analysis. After the projectile has fully penetrated the armor, the "*pushed aside*" yarns tend to recoil. The yarn recoiling process reduces both the size of the penetration hole and the extent of residual lateral displacements in the fabric, Figs. 9d and 10d, respectively. Despite these discrepancies the overall final sizes of the penetration hole are comparable in the two analyses and, more importantly, the residual velocities of the projectile obtained in the two analyses (290.2 m/s in the case of the yarn-level and 289.2 m/s in the case of the unit-cell based FEM analysis) are quite comparable.

In regard to the effect of friction on the fabric deformation and failure behavior in the case of the yarn-level FEM analysis, Figs. 7a–d and 9a–d, the following main observations are made:

(a) No significant changes are introduced initially in the temporal evolution and the spatial distribution of the transverse-deflection wave due to elimination of the yarn/yarn and the projectile/fabric friction; and
(b) The structure of the fabric (including its deformation and failure) in the impact region and in the nearby surrounding regions is greatly affected in the case of zero yarn/yarn and projectile/fabric friction conditions.

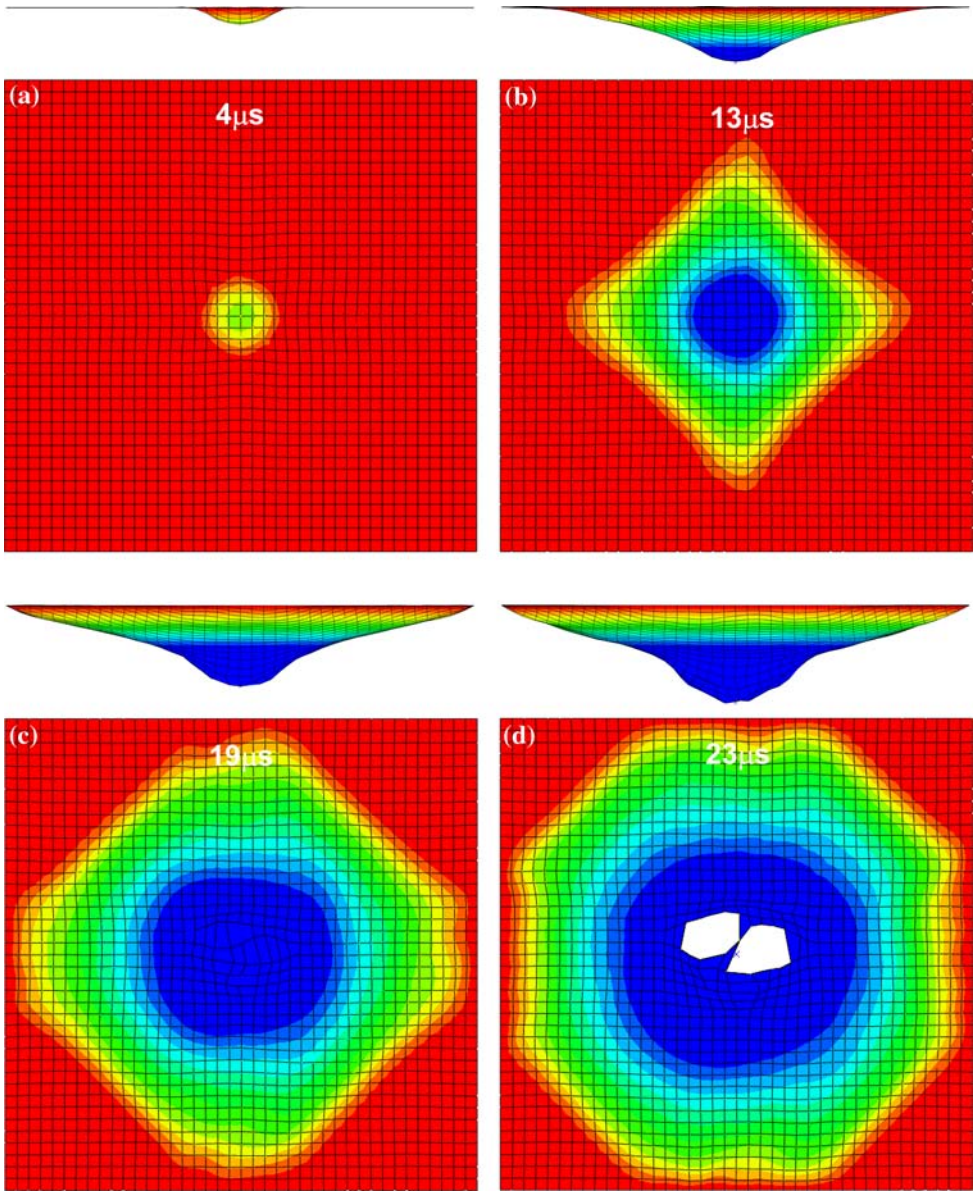

Fig. 10 The temporal evolution of deformation in the fabric for the unit-cell based FEM model under the yarn/yarn $\mu_{y/y}$ and projectile/fabric $\mu_{p/f}$ friction coefficients of 0.0. Contour bands correspond to different values of the transverse displacement, i.e., the displacements normal to the fabric surface. All four fabric edges are fixed

Specifically, in the zero-friction case, yarns were substantially displaced in the in-plane directions away from the center of impact. This finding can be readily explained by the fact that the friction at the yarn crossovers provides resistance to the relative tangential motion of the yarns, while such resistance is absent in the zero-friction case. Consequently, in the zero-friction case yarns impacted by the projectile are pushed outward, a fewer number of yarns are broken and the projectile manages to penetrate the fabric mainly by *"wedging"* through it.

A final examination of the corresponding results displayed in Figs. 9a–d and 10a–d suggests that, considering the fact that the FEM mesh is significantly finer and can capture more details in the case of the yarn-based FEM analyses, the overall agreement between the two analyses relative to the extent of deformation and damage in the armor can be deemed as slightly less satisfactory than in the case when friction is present at the yarn/yarn crossovers and projectile/fabric contact surfaces, Figs. 7a–d to 8a–d. The results displayed in Figs. 7–10 were obtained under the projectile velocity of 300 m/s. A similar level of agreement between the corresponding results obtained in the two FEM analyses was obtained when the projectile velocity was doubled or halved relative to this value.

Fabric's energy absorption potential

In this section, temporal evolutions of the three main energy-absorbing mechanisms (i.e., yarn-strain energy,

yarn-kinetic energy and frictional-sliding losses) are compared for the two types of FEM analyses under the two types of frictional conditions. The corresponding results for the two types of FEM analyses are displayed in Figs. 11a,b and 12a,b, respectively. In the figures the quantities displayed along the vertical axis are all normalized by the corresponding maximum projectile energy loss. Also, the residual projectile velocities are indicated and their comparison suggests a quite good agreement between the corresponding values obtained using the two analyses. A simple comparison of the results displayed in Figs. 11a,b and 12a,b reveals that:

(a) While frictional sliding in general makes a relatively minor contribution to the overall energy absorption capacity of the armor, a somewhat larger contribution of the frictional-sliding losses is present in the case of the yarn-level based analysis, Fig. 11a versus Fig. 12a. This finding is consistent with the fact that, in the case of the unit-cell based analysis, yarn/yarn friction is not included explicitly and does not contribute to the frictional-sliding losses;

(b) The yarn strain-energy contributions predicted by the two FEM analyses are quite comparable under the same frictional conditions. A similar conclusion can

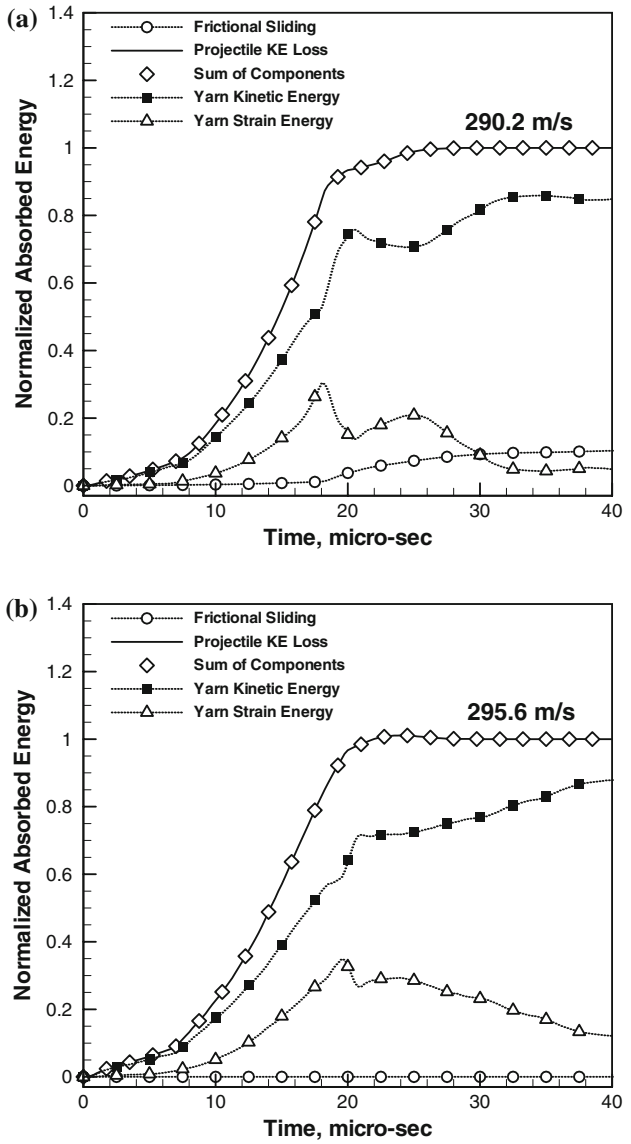

Fig. 11 The effect of yarn/yarn $\mu_{y/y}$ and projectile/fabric $\mu_{p/f}$ friction coefficients on the temporal evolution of projectile's kinetic-energy loss and on different energy-absorbing mechanisms in the fabric obtained using the yarn-level FEM model: (**a**) $\mu_{y/y} = \mu_{p/f} = 0.5$ and (**b**) $\mu_{y/y} = \mu_{p/f} = 0.0$

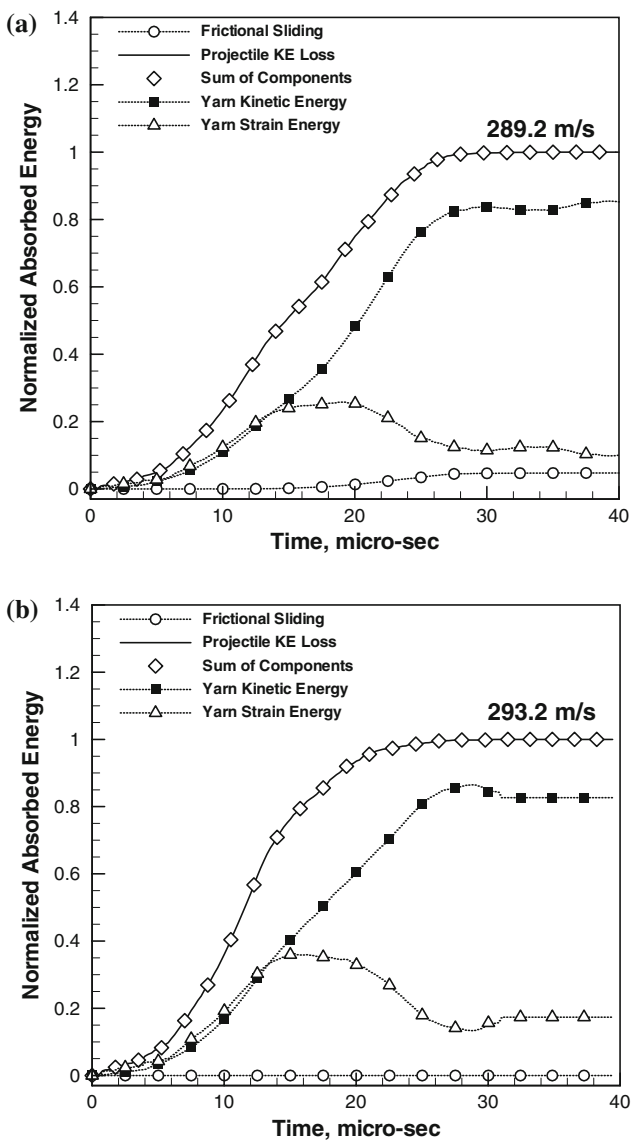

Fig. 12 The effect of yarn/yarn $\mu_{y/y}$ and projectile/fabric $\mu_{p/f}$ friction coefficients on the temporal evolution of projectile's kinetic-energy loss and on different energy-absorbing mechanisms in the fabric obtained using the unit-cell based FEM model: (**a**) $\mu_{y/y} = \mu_{p/f} = 0.5$ and (**b**) $\mu_{y/y} = \mu_{p/f} = 0.0$

be drawn regarding the yarn-kinetic energy contributions under the same frictional conditions;

(c) In the case of the yarn-level FEM analysis, the full-penetration time (defined as a time when the projectile reaches its final velocity) is slightly greater ($\sim$26 μs) in the presence of friction, Fig. 11a, than ($\sim$23 μs) in the zero-friction case, Fig. 11b. This finding is related to the fact that in the absence of friction the projectile can wedge through the fabric, while in the presence of friction more yarn failure is required before the projectile can reach its residual velocity. In the case of the unit-cell based FEM analysis, similar full-penetration time differences are seen but to a lesser extent since no "*wedge through*" effect can take place, Fig. 12a and b. Under the same frictional conditions, the full-penetration times as predicted by the two FEM analyses are comparable;

(d) As mentioned in point (a), the contribution of the frictional sliding mechanism to energy absorption is relatively small. However, the presence of friction itself enhances projectiles' kinetic-energy absorption via yarn straining and acceleration and, thus, increases the energy-absorption capacity of the fabric. This finding is based on a comparison between the residual projectile velocities in the friction case, Figs. 11a and 12a and in the zero-friction case, Figs. 11b and 12b;

(e) As the projectile begins to interact with the fabric, the contributions of yarn straining to the energy-absorption process increases. Once the projectile starts to penetrate the armor, further yarn straining ceases to occur. At the same time, the relative kinetic energy component of the yarns increases (due to yarn recoiling) and likewise the frictional-sliding component of the total yarn energy increases; and

(f) The extent of agreement between the two FEM analyses regarding the energy absorption capacity of armor under the projectile velocity of 300 m/s as seen in Figs. 11a,b and 12a,b was also observed under different initial projectile velocities.

The effect of far-field boundary conditions

The results presented and discussed in the section "Clamped fabric edges boundary condition" pertain to the case of fixed boundary conditions applied to all four edges of the armor. It is generally found that the nature (free versus fixed) of boundary conditions affects the ballistic response of the armor and its ability to absorb kinetic energy as well as it affects the relative contributions of various energy-absorbing mechanisms [e.g., 10–13]. The results presented and discussed in the section "Clamped fabric edges boundary condition" show that the meso-scale unit-cell based material model can reasonably well account for the deformation/failure behavior and the energy-absorbing capacity of a plain-woven single-ply fabric under fixed boundary conditions being applied to all four fabric edges. In this section, a comparison is made between the corresponding results obtained using the yarn-level FEM and unit-cell based FEM analyses under the two types of boundary conditions given below.

Figure 13a–d shows the deformed configuration obtained using the yarn-level FEM analysis for fabric armor at a fixed post-impact time of 23 μs for the two frictional conditions when: (a) two opposite edges are fixed and the other two are free, Fig. 13a and b, respectively; and (b) when all four edges are free, Fig. 13c and d. The corresponding results obtained using the unit-cell based FEM analysis are displayed in Fig. 14a–d. A comparison of the results displayed in Figs. 13a–d and 14a–d reveals that the agreement between the two is reasonable. Specifically:

(a) Under the boundary conditions corresponding to two fixed and two free edges, Figs. 13a,b and 14a–d, there is good agreement with respect to the "*bowing-in*" response of the free edges and the extent of fabric damage in the region directly impacted by the projectile. However, the spatial distributions of the lateral displacements and damage are quite different in the two analyses. That is, in the case of yarn-level FEM analysis and in particular in the absence of friction, the yarn transverse deflections are more highly localized in the region surrounding the point of impact. This finding is not quite surprising since in the yarn-level FEM analysis, the (principal) yarns have the ability to move sideways to avoid the projectile and can also be pulled out (since only the yarn/yarn friction opposes this process). In the case of the unit-cell based FEM analysis, the "yarns" are all merged into continuous unit cells and as discussed in the section "Clamped fabric edges boundary condition" they do not have similar moving latitudes to the ones described above;

(b) Under the boundary conditions corresponding to four free edges, Figs. 13c,d and 14a–d, there is again good agreement with respect to the "*bowing-in*" response of the free edges and the side-view profile of the transverse deflections (particularly in the presence of friction). Also, fabric damage is absent in both analyses. However, the spatial distributions of the transverse deflections are slightly different in the two analyses in the presence of friction, Figs. 13c and 14c. Specifically, the transverse-wave front acquires a square-shape in the yarn-level case, Fig. 13c, while this wave-front shape is more circular in the case of the unit-cell analysis, Fig. 14c. In the absence of

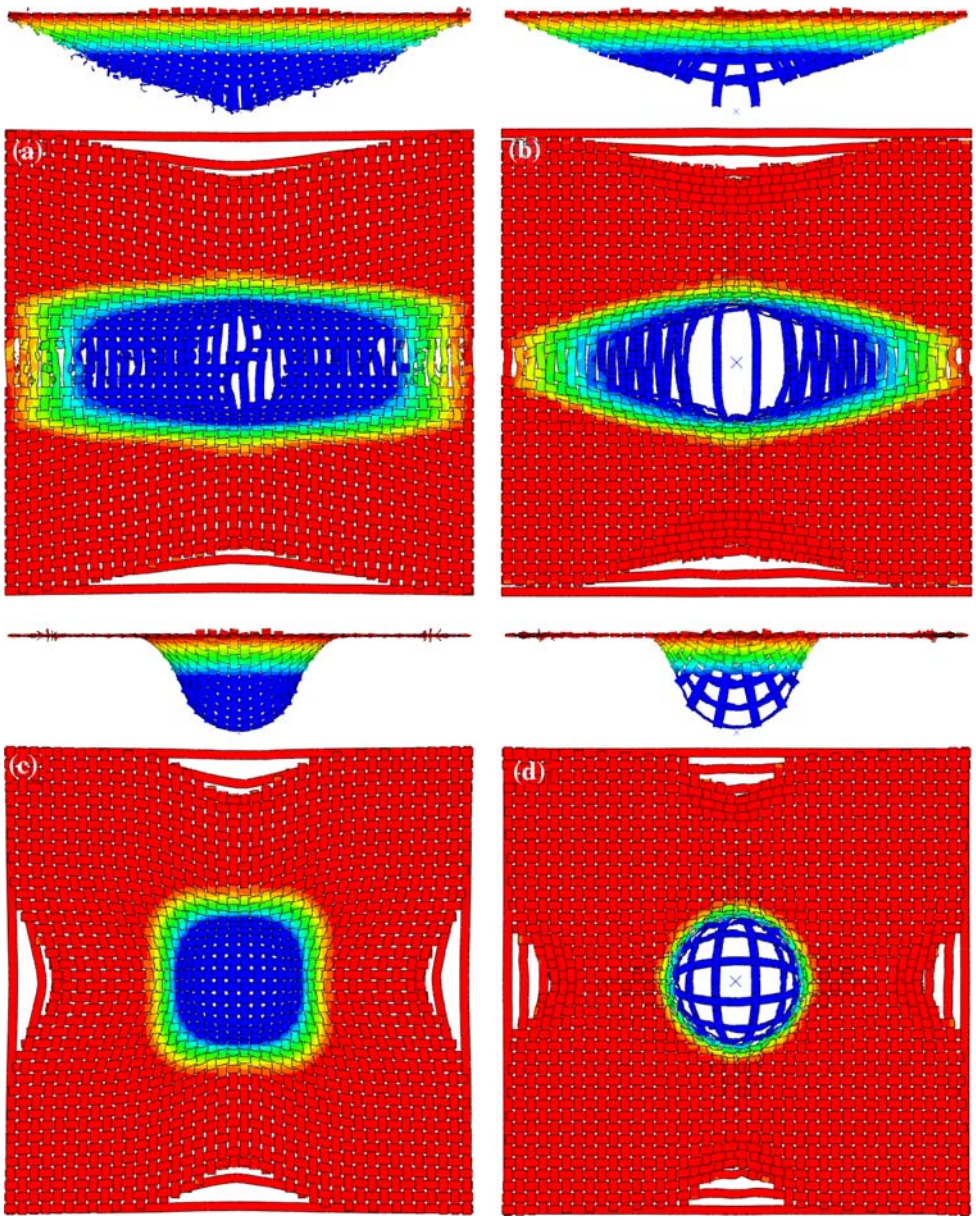

Fig. 13 The deformation state of the fabric at 23 μs for the yarn-level FEM model under the yarn/yarn $\mu_{y/y}$ and projectile/fabric $\mu_{p/f}$ friction coefficients of: (**a**) and (**c**) 0.5; and (**b**) and (**d**) 0.0. Boundary conditions: (**a**) and (**b**) Left/right fabric edges are fixed; and (**c**) and (**d**) All four edges are free

friction, on the other hand, the transverse wave front shape is nearly circular in both analyses, but due to higher lateral mobility of the yarns transverse deflections are highly localized in the region immediately surrounding the point of impact in the case of the yarn-level analysis, Fig. 13d versus Fig. 14d; and

(c) The energy absorption capacity of the fabric under the two types of boundary conditions analyzed in this section, as predicted by the two analyses (results not shown for brevity), are quite comparable.

Based on the findings presented in this and the previous section, one may conclude that the proposed meso-scale unit-cell based material model for a plain-woven single-ply fabric can reasonably well account for the behavior of fabric under different boundary conditions, and yarn/yarn and projectile/fabric friction conditions when subjected to ballistic loading.

Summary and conclusions

Based on the material-model development procedure utilized and the results of the subsequent computational analyses, the following main summary remarks and conclusions can be drawn:

1. A simple meso-scale unit-cell based material model for plain-woven single-ply fabric armor is developed and implemented in a user-material subroutine suitable for use with commercial explicit finite-element programs.

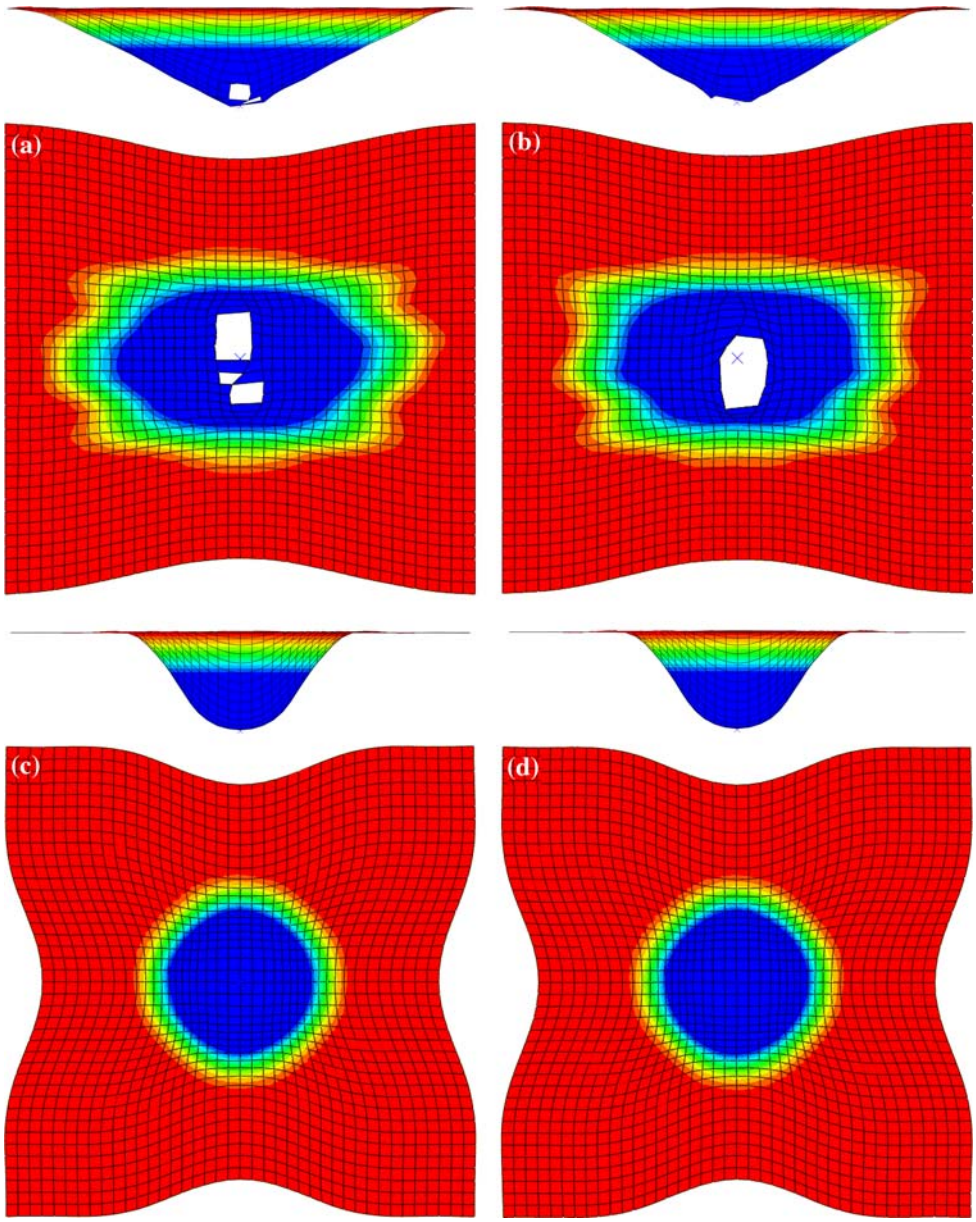

Fig. 14 The deformation state of the fabric at 23 μs for the unit-cell based FEM model under the yarn/yarn $\mu_{y/y}$ and projectile/fabric $\mu_{p/f}$ friction coefficients of: (**a**) and (**c**) 0.5; and (**b**) and (**d**) 0.0. Boundary conditions: (**a**) and (**b**) Left/right fabric edges are fixed; and (**c**) and (**d**) all four edges are free

2. The user-material subroutine is coupled with the ABAQUS/Explicit finite-element program and used in a series of transient non-linear dynamic analyses of a plain-woven single-ply fabric armor impacted by a spherical steel projectile in order to test and validate the material model.
3. The results obtained in a finite-element analysis in which the user-material subroutine is used are compared their counterparts obtained in a computationally more-costly FEM model in which yarn weaving is accounted for explicitly under different boundary conditions applied to the edges of the fabric test patch, and under different yarn/yarn and projectile/fabric projectile conditions.
4. This comparison established that, in general, that the proposed material model for the plain-woven single-ply fabric can reasonably well account for the fabric behavior when subjected to ballistic impact loading.
5. The agreement is somewhat better when friction is assumed to exist between the contacting yarns and the projectile and fabric than in the zero-friction case. This finding was related to the limitations of the current material model to fully account for the lateral motion of the yarns.
6. To further validate the meso-scale unit-cell based material model for single-ply ballistic fabric developed in the present work, a set of experimental field tests of the ballistic performance of the fabric in question will be carried out and reported in our future work.

Acknowledgements The material presented in this article is based on work supported by the U.S. Army/Clemson University Cooperative Agreements W911NF-04-2-0024 and W911NF-06-2-0042. The authors are indebted to Dr. Fred Stanton for the support and a continuing interest in the present work.

References

1. MIT Nano Soldier Institute for Soldier Nanotechnologies Massachusetts Institute of Technology, Cambridge, MA, http://www.web.mit.edu/ISN/
2. King MJ, Jearanaisilawong P, Socrate S (2005) Int J Solids Struct 42:3867. doi:10.1016/j.ijsolstr.2004.10.030
3. Wittman RE, Rolsten RF (1967) Armor of men and aircraft. In: 12th national SAMPE symposium
4. The Interceptor System US Marine Corps (http://www.marines.mil/marinelink/image1.nsf/lookup/200532317129?opendocument)
5. Roylance D, Wang SS (1980) Penetration mechanics of textile structures ballistic materials and penetration mechanics. Elsevier, Amsterdam, p 273
6. Shim VPW, Lim CT, Foo KJ (2001) Int J Impact Eng 25:1. doi:10.1016/S0734-743X(00)00038-5
7. Lim CT, Shim VPW, Ng YH (2003) Int J Impact Eng 28:13. doi:10.1016/S0734-743X(02)00031-3
8. Shahkarami A, Vaziri R, Poursartip A, Williams K (2002) A numerical investigation of the effect of projectile mass on the energy absorption of fabric panels subjected to ballistic impact. In: Proceedings of the 20th international symposium on ballistics, pp 802–809
9. Johnson GR, Beissel SR, Cunniff PM (1999) A computational model for fabrics subjected to ballistic impact. In: Proceedings of the 18th international symposium on ballistics, San Antonio, vol 2, pp 962–969
10. Billon HH, Robinson DJ (2001) Int J Impact Eng 25:411. doi:10.1016/S0734-743X(00)00049-X
11. Shockey DA, Erlich DC, Simons JW (2000) Improved barriers to turbine engine fragments, US department of transportation. SRI International, Menlo Park
12. Duan Y, Keefe M, Bogetti TA, Cheeseman BA (2005) Int J Impact Eng 31:996. doi:10.1016/j.ijimpeng.2004.06.008
13. Duan Y, Keefe M, Bogetti TA, Cheeseman BA (2005) Int Compos Struct 68:331. doi:10.1016/j.compstruct.2004.03.026
14. Duan Y, Keefe M, Bogetti TA, Cheeseman BA, Powers B (2006) Int J Impact Eng 32:1299. doi:10.1016/j.ijimpeng.2004.11.005
15. Duan Y, Keefe M, Bogetti TA, Powers B (2006) Int J Mech Sci 48:33. doi:10.1016/j.ijmecsci.2005.09.007
16. Zhang GM, Batra RC, Zheng J (in press) Compos Part B
17. Kawabata S, Niwa M, Kawai H (1973) J Text Inst 64:21
18. Kawabata S, Niwa M, Kawai H (1973) J Text Inst 64:47
19. Kawabata S, Niwa M, Kawai H (1973) J Text Inst 64:62
20. Ivanov I, Tabiei A (2004) Int J Numer Methods Eng 61:1565. doi:10.1002/nme.1113
21. Boisse P, Zouari B, Gasser A (2005) Compos Sci Technol 65:429. doi:10.1016/j.compscitech.2004.09.024
22. Peng X, Cao J (2002) Compos Part B Eng 33:45. doi:10.1016/S1359-8368(01)00052-X
23. Shahkarami A, Vaziri R (2007) Int J Impact Eng 34:104. doi:10.1016/j.ijimpeng.2006.06.010
24. Scott BR, Yen CF (2005) Analytic design trends in fabric armor. In: Proceedings of the 22nd international ballistics symposium, pp 752–760
25. Simplex Method: in Numerical Recipes, http://library.lanl.gov/numerical/index.html
26. Version ABAQUS 6.7.4, User Documentation, Dassault Systems, 2007
27. King MJ (2006) A continuum constitutive model for the mechanical behavior of woven fabrics including slip and failure. Ph.D. Thesis, MIT
28. Grujicic M, Arakere G, He T, Gogulapati M, Cheeseman BA (2008) J Mater: Des Appl (accepted)
29. Tan VBC, Lim CT, Cheong CH (2003) Int J Impact Eng 28:207